**Astronomy
&
Astrophysics**

An analysis of spectroscopic, seismological, astrometric, and photometric masses of pulsating white dwarf stars

Leila M. Calcaferro[1,2], Alejandro H. Córsico[1,2,*], Murat Uzundag[3], Leandro G. Althaus[1,2],
S. O. Kepler[4], and Klaus Werner[5]

[1] Grupo de Evolución Estelar y Pulsaciones, Facultad de Ciencias Astronómicas y Geofísicas, Universidad Nacional de La Plata, Paseo del Bosque s/n, 1900 La Plata, Argentina
[2] Instituto de Astrofísica La Plata, CONICET-UNLP, Paseo del Bosque s/n, (1900) La Plata, Argentina
[3] Institute of Astronomy, KU Leuven, Celestijnenlaan 200D, 3001 Leuven, Belgium
[4] Instituto de Física da Universidade Federal do Rio Grande do Sul, 91501-970 Porto Alegre, Brazil
[5] Institut für Astronomie und Astrophysik, Kepler Center for Astro and Particle Physics, Eberhard Karls Universität, Sand 1, 72076 Tübingen, Germany

Received 1 May 2024 / Accepted 5 September 2024

ABSTRACT

Context. A central challenge in the field of stellar astrophysics lies in accurately determining the mass of stars, particularly when dealing with isolated ones. However, for pulsating white dwarf stars, the task becomes more tractable due to the availability of multiple approaches such as spectroscopy, asteroseismology, astrometry, and photometry, each providing valuable insights into the mass properties of white dwarf stars.

Aims. Numerous asteroseismological studies of white dwarfs have been published, focusing on determining stellar mass using pulsational spectra and comparing it with spectroscopic mass, which uses surface temperature and gravity. The objective of this work is to compare these mass values in detail and, in turn, to compare them with the mass values derived using astrometric parallaxes or distances and photometry data from *Gaia*, employing astrometric and photometric methods.

Methods. Our analysis involves a selection of pulsating white dwarfs with different surface chemical abundances that define the main classes of variable white dwarfs. We calculated their spectroscopic masses, compiled seismological masses, and determined astrometric masses. We also derived photometric masses, when possible. Subsequently, we compared all the sets of stellar masses obtained through these different methods. To ensure consistency and robustness in our comparisons, we used identical white dwarf models and evolutionary tracks across all four methods.

Results. The analysis suggests a general consensus among the four methods regarding the masses of pulsating white dwarfs with hydrogen-rich atmospheres, known as DAV or ZZ Ceti stars, especially for objects with masses below approximately $0.75\,M_\odot$, although notable disparities emerge for certain massive stars. For pulsating white dwarf stars with helium-rich atmospheres, called DBV or V777 Her stars, we find that astrometric masses generally exceed seismological, spectroscopic, and photometric masses. Finally, while there is agreement among the sets of stellar masses for pulsating white dwarfs with carbon-, oxygen-, and helium-rich atmospheres (designated as GW Vir stars), outliers exist, where mass determinations by various methods show significant discrepancies.

Conclusions. Although a general agreement exists among different methodologies for estimating the mass of pulsating white dwarfs, significant discrepancies are prevalent in many instances. This shows the need to redo the determination of spectroscopic parameters and the parallax and/or improve asteroseismological models for many stars.

Key words. asteroseismology – surveys – stars: evolution – stars: interiors – stars: oscillations – white dwarfs

1. Introduction

In stellar astrophysics, the mass of stars stands as a fundamental quantity, as it shapes the entire life cycle of stars, from their birth to their death (see, e.g., Hansen et al. 2004; Kippenhahn et al. 2013). Stellar masses cover a vast range, extending from approximately 0.08 to about 150 times the mass of the Sun ($M_\odot$) and even beyond. The accurate determination of stellar mass is pivotal for a myriad of studies of formation, evolution, ages, and distances of stellar populations, as well as investigations into the chemical composition of stars, supernovae, asteroseismology, exoplanets, and more. Nevertheless, precisely measuring stellar mass poses challenges, particularly for isolated stars lacking companions. For an exhaustive exploration of the various methodologies employed in measuring stellar mass, we

recommend consulting the comprehensive review article by Serenelli et al. (2021) and the references provided therein.

White dwarf (WD) stars represent the predominant fate among stars in the Universe (e.g. Althaus et al. 2010; Saumon et al. 2022). In fact, most stars whose progenitor masses are below $8-10.5\,M_\odot$, depending on metallicity, will end their evolution as WDs (e.g. Doherty et al. 2014). The observed mass range of WDs spans from approximately $0.17\,M_\odot$ (SDSS J091709.55+463821.8; Kilic et al. 2007) to around $1.35\,M_\odot$ (ZTF J190132.9+145808.7; Caiazzo et al. 2021). The precise measurement of WD masses is pivotal in numerous astrophysical studies. It plays a crucial role in the assessment of the initial-to-final mass relationship of WDs (Weidemann 1977; Catalán et al. 2008; El-Badry et al. 2018; Cummings et al. 2019). Additionally, WD masses are crucial to computing the WD luminosity function, which serves as a valuable tool to

infer the age, structure, and evolution of the Galactic disc, as well as the nearest open and globular clusters (Fontaine et al. 2001; Bedin et al. 2009; García-Berro et al. 2010; Bedin et al. 2015; Campos et al. 2013, 2016; García-Berro & Oswalt 2016; Kilic et al. 2017).

In select situations, the mass of a WD can be measured directly using model-independent methods. This is notably observed in astrometric WD binaries that possess precise orbital parameters that allow a dynamic determination of their mass (e.g. Bond et al. 2015, 2017a,b) as well as in detached eclipsing binaries (e.g. Parsons et al. 2017) and by means of the gravitational redshift of spectral lines (e.g. Pasquini et al. 2019). In the vast majority of cases, however, WDs are discovered in isolation, necessitating the estimation of their stellar masses through model-dependent methods. The key methods we discuss in this study include the determination of the spectroscopic mass, the seismological mass, the astrometric mass, and the photometric mass.

The spectroscopic mass of WDs is derived using the effective temperature and surface gravity, acquired by fitting the atmosphere models χ^2 to stellar spectra with line profiles. This is called the spectroscopic technique, and it has historically been the most successful technique to obtain the atmospheric parameters T_{eff} and $\log g$ of WDs. These parameters are commonly referred to as spectroscopic T_{eff} and $\log g$ (Bergeron et al. 1992; Liebert et al. 2005; Tremblay & Bergeron 2009). The process of assessing the stellar mass from T_{eff} and $\log g$ involves the utilisation of evolutionary tracks of WDs in the gravity versus effective temperature plane, often referred to as 'Kiel diagrams'. An illustrative example of the derivation of spectroscopic masses for a large sample of WDs based on $\log g$ and T_{eff} can be found in the research conducted by Kleinman et al. (2013).

The seismological masses of WDs are determined by asteroseismology, a technique that involves comparing the pulsation spectra observed in the g (gravity) mode in variable WDs with the theoretical spectra calculated on the appropriate grids of the WD models (Winget & Kepler 2008; Fontaine & Brassard 2008; Althaus et al. 2010; Córsico et al. 2019a). Continuous observations from space, exemplified by missions such as CoRoT, *Kepler*, and TESS, have significantly advanced the field of WD asteroseismology (Córsico 2020, 2022; Romero et al. 2022, 2023). Asteroseismology has been shown to be effective in obtaining stellar masses of isolated pulsating WDs (Romero et al. 2012; Giammichele et al. 2018). Seismological models can be constructed by fitting individual periods for each pulsating star, which allows for the derivation of the seismological mass. In instances where a constant period spacing is discernible in the observed pulsation spectrum, the seismological mass can also be determined by comparing this period spacing with the uniform period spacings calculated for theoretical models (see, for instance, Kawaler 1987; Córsico et al. 2021). This particular method relies on the spectroscopic effective temperature of the star and its associated uncertainties.

The astrometric masses of WDs can be determined by calculating the theoretical distances of WD models associated with evolutionary tracks of varying masses. This process involves utilising the apparent magnitude of a WD and the absolute magnitude of the models. The calculated theoretical distance for different stellar masses is then compared with the astrometric distance of the WD, derived from its parallax, thus allowing for a mass estimate. The availability of accurate measurements from *Gaia* (Gaia Collaboration 2020) gives this technique particular relevance. It is important to note that the determination of stellar masses for WDs through this method is also dependent on the spectroscopic effective temperature of the star.

Finally, the photometric masses of WDs can be assessed by fitting photometry and astrometric parallaxes or distances, employing synthetic fluxes from model atmospheres, to constrain the WD T_{eff} and radius (Bergeron et al. 1997, 2001, 2019; Gentile Fusillo et al. 2019). The subsequent use of the mass-radius relationships yields the stellar mass. The accurate trigonometric *Gaia* parallax or distance measurements, coupled with large photometric surveys such as the Sloan Digital Sky Survey (SDSS; York et al. 2000) and the Panoramic Survey Telescope and Rapid Response System (Pan-STARRS; Chambers et al. 2016), have turned the photometric method into a very accurate technique to measure the mass of isolated WDs (see, e.g., Bergeron et al. 2019; Genest-Beaulieu & Bergeron 2019a; Gentile Fusillo et al. 2019; Tremblay et al. 2019).

Many asteroseismological analyses providing the stellar masses of pulsating WDs have been carried out so far, and their estimates have been compared with spectroscopic or photometric determinations of stellar mass. It has been concluded that these sets of masses generally agree with each other. However, a detailed comparative analysis has not been carried out until now. The main objective of the present analysis is to determine to what extent the different methods used to derive the stellar mass of isolated pulsating WDs are consistent with each other. In this paper, we undertake a comparative analysis of WD stellar masses, employing the methods previously described. In particular, we made extensive use of astrometric distance estimates provided by *Gaia*, which allowed us to make a new estimate of the stellar mass of isolated WDs. Our approach involves using identical evolutionary tracks and model WDs across all procedures. Specifically, for evaluating spectroscopic, astrometric, and photometric masses, we employed the same evolutionary tracks associated with the sets of WD stellar models utilised in asteroseismological analyses to derive seismological masses. This strategy ensures consistency and robustness when comparing the four stellar mass estimates.

The paper is structured as follows. In Section 2, we provide a brief overview of the samples of stars analysed in this study. The specific objects considered are listed in Appendix A. Section 3 outlines the four methods used to derive stellar mass, while Section 4 is dedicated to presenting a comparative analysis of the mass determinations obtained for our sample of stars. We discuss potential reasons for discrepancies among the different mass determinations in Section 5. Finally, we offer a summary and draw conclusions from our findings in Section 6.

2. Samples of stars

We selected samples of three types of pulsating WD stars: DAV[1] (spectral type DA, with hydrogen-rich atmospheres), DBV (spectral type DB, with helium-rich atmospheres), and GW Vir (spectral types PG 1159 and [WC], with oxygen-, carbon- and helium-rich atmospheres) stars, respectively. Within the category of GW Vir stars, we include DOV-type stars (GW Vir stars that lack a nebula) and PNNV-type stars (GW Vir stars that are still surrounded by a nebula). The stars discussed in this study have been seismologically analysed using evolutionary models generated with the LPCODE evolutionary code (Althaus & Córsico 2022) and pulsation periods of g modes

---

[1] We do not consider in this study the pulsating low-mass and extremely low-mass helium-core WDs (also known as ELMVs; see, e.g., Córsico et al. 2019a), that are also hydrogen-rich atmosphere WDs, the results of which will be presented in a separate work (Calcaferro et al., in prep.).

calculated with the LP-PUL pulsation code (Córsico & Althaus 2006), both developed by the La Plata Group[2]. In Tables A.1, A.2, and A.3, we present the details of the stars included in our study. The tables provide information such as star names, equatorial coordinates, apparent magnitude V, and DR3 *Gaia* apparent magnitudes G, G_{BP}, and G_{RP}. In addition, they list spectral type, spectroscopic effective temperature, and surface gravity, DR3 *Gaia* parallax (Gaia Collaboration 2023), and geometric distance from Bailer-Jones et al. (2021). For DBV and GW Vir stars (Tables A.2, and A.3), we include an extra column that indicates interstellar extinction (A_V). It should be noted that the GW Vir star PG 2131+066 lacks parallax data from *Gaia*, so we could not obtain the distance from Bailer-Jones et al. (2021). Instead, we include the distance derived by Reed et al. (2000) using the spectroscopic parallax of the nearby M star to which PG 2131+066 appears to compose a binary.

The extinction values listed in Tables A.2 and A.3 were obtained using the following approach. We used the Python package `dustmaps`[3] to derive reddening values $E(B - V)$ for each target location in the sky, based on the 3D reddening map `Bayestar17` (Green et al. 2018). The central $E(B-V)$ value was directly extracted from these maps, serving as our primary estimate of extinction at each target location. Furthermore, we determined the upper and lower percentiles of the extinction values (typically at 84.1% and 15.9%, respectively) to establish uncertainty limits. Subsequently, we computed the error in reddening by measuring the difference between the central value and the upper and lower percentiles. We then calculated the extinction values for the V band (A_V) using the formula $A_V = R_V E(B-V)$, using $R_V = 3.2$ (Fitzpatrick 2004). For DBV stars located below a declination of -30 deg, we used the 2D 'SFD' dust maps within the `dustmaps` package, based on the catalogue compiled by Schlegel et al. (1998), as the `Bayestar17` catalogue does not cover this range. Our A_V values for GW Vir stars closely match those reported by Sowicka et al. (2023), which is reasonable given that both sets of extinctions were derived from the `Bayestar17` map.

Furthermore, we used `Bayestar17` to determine the extinction values for DAVs (not included in Table A.1) and compared them with the values obtained from the Montreal WD database (Dufour et al. 2017). The results showed a strong agreement between the two sets of values. Due to the negligible impact of extinction on DAVs owing to their proximity to the Sun, we did not account for it in our calculations when determining astrometric masses.

It is widely recognised that DA WDs are formed with a range of hydrogen (H) envelope thicknesses rather than a single value, spanning the range $-14 \lesssim \log(M_H/M_\star) \lesssim -3$. The stellar radius and surface gravity of the DA WDs are significantly influenced by the thickness of the H envelope. As a result, the evolutionary tracks in the $T_{\rm eff}$ versus $\log g$ diagram for a given stellar mass vary, with models featuring thinner H envelopes displaying higher gravities (Romero et al. 2019b). Although spectroscopic mass tabulations of DA WDs are commonly found, it is important to note that these values are derived from evolutionary tracks corresponding to DA WD models with 'canonical' envelopes, representing the thickest possible H envelopes. We have observed a recurring error in several asteroseismological studies of DAVs, where seismological masses are often compared with spectroscopic masses. This error arises from comparing seismological masses derived from WD models with

varying thicknesses of H envelopes, ranging from thick (canonical) to thin, with spectroscopic masses obtained from evolutionary tracks associated with WD models featuring only canonical H envelopes. This comparison is evidently incorrect.

Considering the various potential thicknesses of the H envelope, the determination of the stellar mass of DA WDs becomes degenerate without any external constraints. To simplify our analysis and avoid complications, we focused exclusively on studying DAVs in which asteroseismological models – the DA WD models that most accurately replicate the observed periods – are characterised by canonical H envelopes. This approach significantly reduces the number of DAVs available for our analysis. For DBVs and GW Vir stars, we disregard the possibility of thinner He and He/C/O envelopes, respectively, than the canonical ones.

3. Mass derivation

In this section, we describe the methods that we use to determine the mass of selected DAV, DBV, and GW Vir stars (Tables A.1, A.2, and A.3). It is important to clarify that the spectroscopic, seismological, and astrometric masses are not entirely independent, since the methods to obtain them rely on the effective temperature ($T_{\rm eff}$) derived from spectroscopy. Since the photometric method determines $T_{\rm eff}$ as part of its own fitting process, the photometric mass is independent of the spectroscopic $T_{\rm eff}$, at variance with the other methods. Furthermore, it is crucial to highlight that all four sets of masses are model-dependent. Spectroscopic masses are derived from observed spectra, but are based on atmospheric models to determine $T_{\rm eff}$ and $\log g$, and WD evolutionary tracks of different masses to derive the stellar mass. Seismological masses are obtained from measuring the pulsation periods of g modes using photometric techniques, but they depend on the evolutionary pulsation models of WDs and the specific asteroseismological technique employed (e.g. period fits using different quality functions). Lastly, both astrometric and photometric masses are derived from *Gaia*'s parallaxes or their derived distances, combined with apparent magnitudes also measured by *Gaia*. However, these methods also rely on the modelling: the astrometric method uses evolutionary tracks that provide luminosity in terms of $T_{\rm eff}$ and bolometric corrections derived from atmospheric models that are necessary for converting to absolute magnitudes, while the photometric method depends on theoretical mass-radius relations and synthetic fluxes also derived from atmospheric models. Table 1 provides a summary of the points discussed here.

3.1. Spectroscopic masses

We determined the WD spectroscopic masses by the conventional method, that is, by interpolating the surface parameters $\log g$ and $T_{\rm eff}$ derived with the spectroscopic technique and presented in Tables A.1, A.2 and A.3, on the evolutionary tracks provided by Renedo et al. (2010) (CO-core DA WDs) and Camisassa et al. (2019) (ONe-core ultra-massive DA WDs) for DAVs, Althaus et al. (2009) for DBVs and Miller Bertolami & Althaus (2006) for GW Vir stars. The effective temperature and gravity of most of DAV and DBV stars of our samples were extracted from the tabulations of Córsico et al. (2019a) (see Tables A.1 and A.2). These parameters have been corrected for 3D effects (Tremblay et al. 2013; Cukanovaite et al. 2018). In the case of GW Vir stars, we extracted the $T_{\rm eff}$ and $\log g$ values from various authors, as indicated in Table A.3. Figures 1, 2, and 3 display these evolutionary

Table 1. Characteristics of the different methods considered in this work to assess the stellar mass of pulsating WDs.

Method of derivation	Observable	Theoretical
Spectroscopy (M_{Spec})	Electromagnetic spectra	Atmosphere models (T_{eff}, $\log g$)
		Evolutionary tracks ($T_{eff} - \log g$ diagrams)
Asteroseismology (M_{Seis})	g-mode periods (Π)	Evolution and pulsation models
	g-mode constant period spacing ($\Delta\Pi$)	T_{eff} and $\log g$ to select seismological models
Astrometry (M_{Astr})	*Gaia*'s parallax or distance (d_{BJ})	Evolutionary tracks ($\log(L_\star/L_\odot)$)
	Gaia's apparent magnitudes (G, G_{BP}, G_{RP})	Atmosphere models (bolometric correction, BC)
		Spectroscopic T_{eff}
Photometry (M_{Phot})	*Gaia*'s parallax or distance (d_{BJ})	Atmosphere models (synthetic fluxes, H_ν)
	Gaia's apparent magnitudes (G, G_{BP}, G_{RP})	Mass-radius relationships ($M_\star - R_\star$)

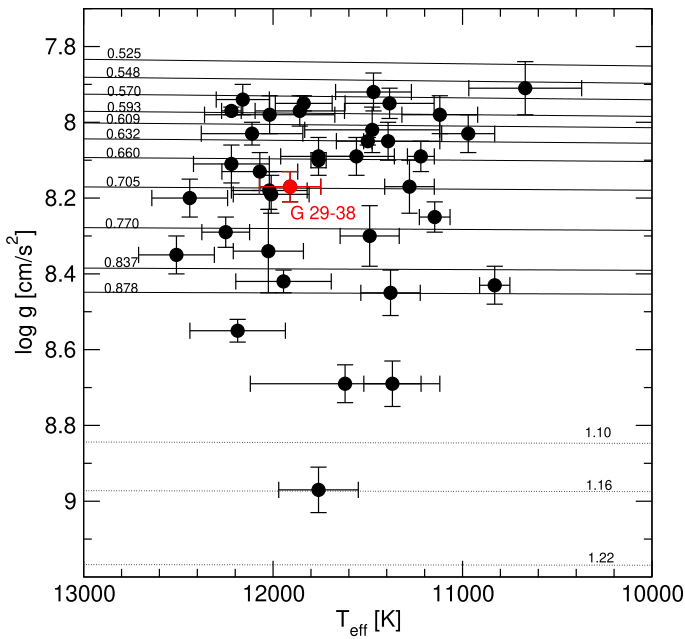**Fig. 1.** Location of the sample of DAV stars considered in this work on the $T_{eff} - \log g$ plane, depicted with black circles. Solid curves show the CO-core DA WD evolutionary tracks from Renedo et al. (2010), and dotted curves display the ultra-massive ONe-core DA WD evolutionary tracks from Camisassa et al. (2019), for different stellar masses. The location of the DAV star G 29−38 is emphasised with a red symbol.

Fig. 2. Location of the sample of DBV stars considered in this work on the $T_{eff} - \log g$ diagram, marked with black circles. Thin solid curves show the CO-core DB WD evolutionary tracks from Althaus et al. (2009) for different stellar masses. The location of the DBV star GD 358 is emphasised with a red symbol.

tracks in the $T_{eff} - \log g$ diagram for each kind of pulsating WD, including the objects analysed in this work. In these figures, we emphasise some representative examples with red symbols and names. For DAVs, we considered only evolutionary tracks corresponding to DA WD models featuring canonical H envelope thicknesses. The derived spectroscopic masses corresponding to DAV, DBV, and GW Vir stars are provided in the second column of Tables B.1, B.2, and B.3, respectively.

3.2. Seismological masses

We collected the seismological masses of pulsating WDs from asteroseismological models derived in the studies by Romero et al. (2012, 2013, 2017, 2019a), Córsico et al. (2019b), Romero et al. (2022, 2023), and Uzundag et al. (2023) for DAVs; Córsico et al. (2012), Bognár et al. (2014), Bell et al. (2019), Córsico et al. (2022b), and Córsico et al. (2022a) for DBVs; and Córsico et al. (2007, 2009), Kepler et al. (2014),
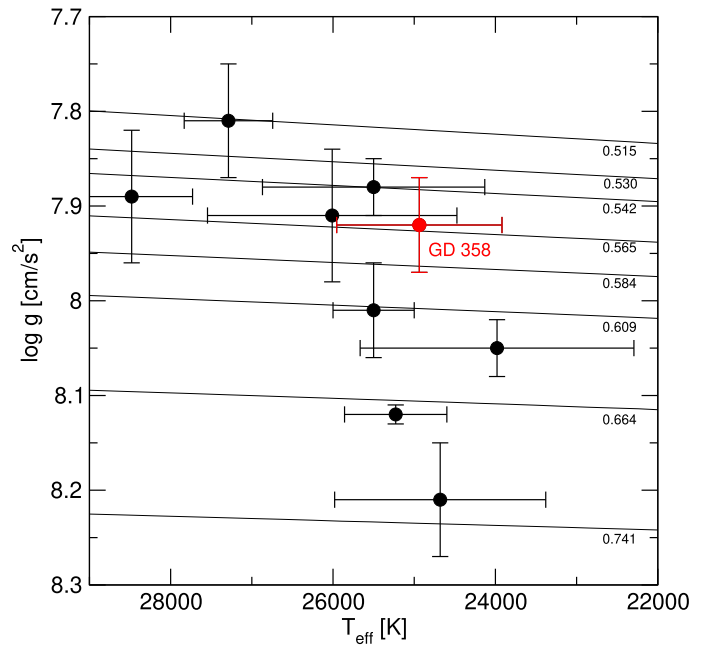
Calcaferro et al. (2016), Córsico et al. (2021), Uzundag et al. (2021), Oliveira Rosa et al. (2022), and Calcaferro et al. (2024) for GW Vir stars. The seismological masses corresponding to DAV, DBV, and GW Vir stars derived from seismological models are provided in the third column of Tables B.1, B.2, and B.3. In the case of DBV and GW Vir stars, in many cases it has also been possible to estimate a seismological mass based on period spacing. These seismological masses are provided in the fourth column of Tables B.2 and B.3. We emphasise that the sample of DAV stars is comprised solely of objects with asteroseismological models characterised by a canonical (thick) H envelope. This explains why our sample of DAVs (Table A.1) is smaller than the total number of DAVs analysed seismologically to date.

3.3. Astrometric masses

We calculated astrometric masses using the following procedure. We built distance curves versus T_{eff} by using Pogson's law, which states that the distance of a star is given by
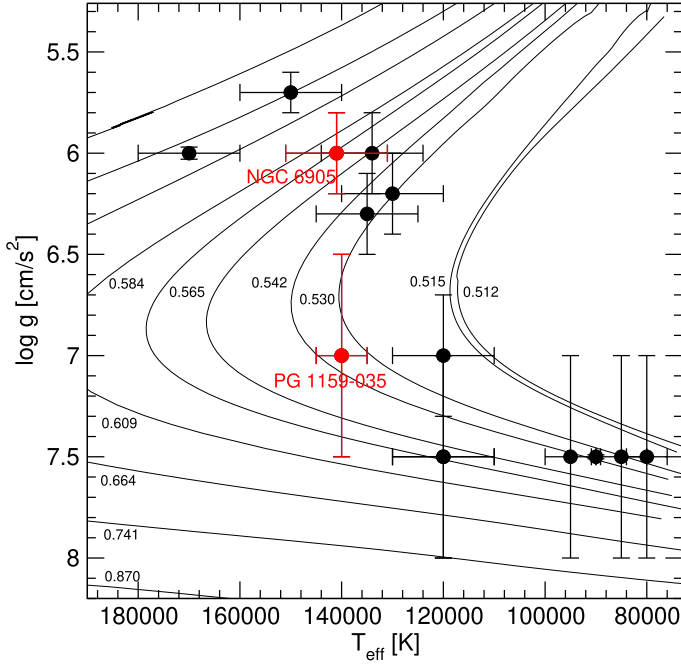
Fig. 3. Location of the sample of GW Vir variable stars considered in this work in the $T_{\mathrm{eff}} - \log g$ plane depicted with black circles. Thin solid curves show the CO-core PG 1159 evolutionary tracks from Miller Bertolami & Althaus (2006) for different stellar masses. The locations of the GW Vir stars PG 1159−035 (DOV type) and NGC 6904 (PNNV type) are marked with red symbols.
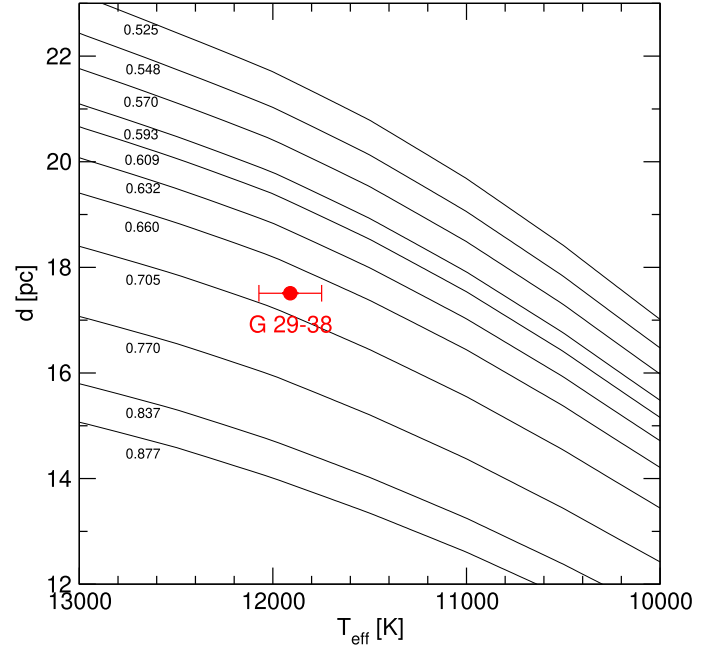

Fig. 4. Distance versus effective temperature curves corresponding to evolutionary sequences of DA WD models extracted from Renedo et al. (2010) with different stellar masses and for the apparent magnitude V of the DAV star G 29−38, whose location is indicated with a red circle with error bars. This star is characterised by $T_{\mathrm{eff}} = 11\,910 \pm 162\,\mathrm{K}$ and $d_{\mathrm{BJ}} = 17.51 \pm 0.01\,\mathrm{pc}$. The uncertainty in the distance is so small that it is contained within the symbol. From linear interpolation, the astrometric mass of G 29−38 is $M_{\mathrm{Astr}} = 0.684^{+0.011}_{-0.014}\,M_{\odot}$.

$\log d = (V - M_V + 5 - A_V)/5$, where V and M_V represent the visual apparent and absolute magnitudes, respectively, and A_V denotes the interstellar absorption in the V band. Using the bolometric correction (BC) from the WD grids of the Montreal Group[4] (Bergeron et al. 1995; Holberg & Bergeron 2006; Bédard et al. 2020), the absolute visual magnitude was calculated as $M_V = M_B - \mathrm{BC}$, where $M_B = M_{B_{\odot}} - 2.5 \log(L_{\star}/L_{\odot})$ and $M_{B_{\odot}} = 4.74$ (Cox 2000). The function $\log(L_{\star}/L_{\odot})$ in terms of T_{eff} for different values of $M_{\star}$ was obtained from the LPCODE WD evolutionary tracks provided by Renedo et al. (2010) (CO-core DA WDs) and Camisassa et al. (2019) (ONe-core ultra-massive DA WDs) for DAVs, Althaus et al. (2009) for DBVs, and Miller Bertolami & Althaus (2006) for GW Vir stars. Following Sowicka et al. (2023), the apparent visual magnitude V was evaluated based on the magnitudes G, G_{BP} and G_{RP} Gaia using the expression

$$V = G + 0.02704 - 0.01424\,(G_{\mathrm{BP}} - G_{\mathrm{RP}})$$
$$+ 0.21560\,(G_{\mathrm{BP}} - G_{\mathrm{RP}})^2$$
$$- 0.01426\,(G_{\mathrm{BP}} - G_{\mathrm{RP}})^3, \tag{1}$$

extracted from Table 5.9 of Gaia DR3 documentation[5]. The uncertainties of G, G_{BP}, and G_{RP} produce errors in V. To estimate the uncertainties ΔG, ΔG_{BP} and ΔG_{RP}, we used the following expressions:

$$\Delta G = 1.089\,\frac{G}{(S/N)},$$
$$\Delta G_{\mathrm{BP}} = 1.089\,\frac{G_{\mathrm{BP}}}{(S/N)},$$
$$\Delta G_{\mathrm{RP}} = 1.089\,\frac{G_{\mathrm{RP}}}{(S/N)}), \tag{2}$$

where (S/N) is approximately equal to the parameter `phot_g_mean_flux_over_error` of the Gaia database[6]. We propagated the errors of G, G_{BP} and G_{RP} to V to obtain ΔV in the usual way (see the fourth column of Tables A.1, A.2, and A.3). We generated curves of d as a function of T_{eff} for each stellar mass $M_{\star}$. We identified the target star based on its specified T_{eff} and the distance extracted from Bailer-Jones et al. (2021) on the d versus T_{eff} diagrams. By interpolating between these curves, we estimated the astrometric mass, M_{Astr}. Each star has its own set of d versus T_{eff} curves, as these curves depend on the star's magnitude V. The resulting astrometric masses are provided in the fifth column of Table B.1 for DAVs, and the sixth column of Tables B.2 and B.3 for DBV and GW Vir stars.

In Fig. 4, we present a $T_{\mathrm{eff}} - d$ diagram illustrating the case of the DAV star G 29−38, while Fig. 5 shows the DBV star GD 358. Furthermore, Figs. 6 and 7 highlight the GW Vir stars PG 1159−035 (DOV type) and NGC 6905 (PNNV type), respectively. For DAVs and DBVs, which are typically in close proximity to the Sun, the uncertainties in the distances provided by Bailer-Jones et al. (2021) are minimal, resulting in error bars that

---

[4] https://www.astro.umontreal.ca/~bergeron/CoolingModels/
[5] https://gea.esac.esa.int/archive/documentation/GDR3/Data_processing/chap_cu5pho/cu5pho_sec_photSystem/

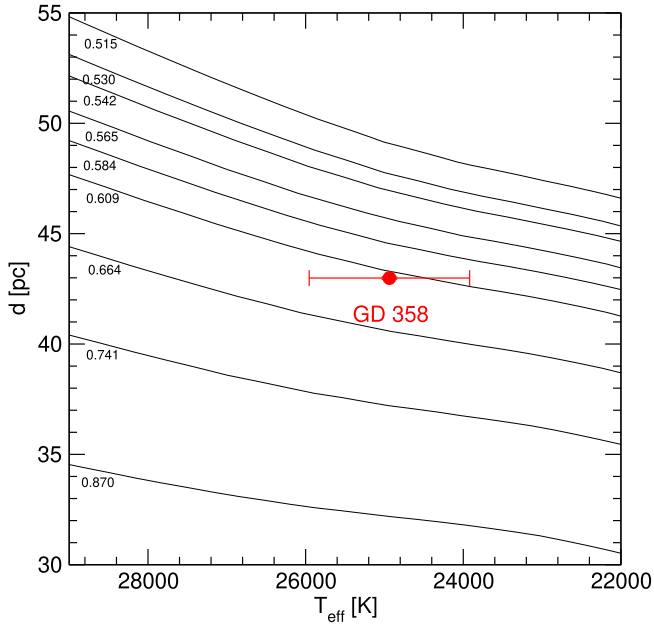[6] https://dc.zah.uni-heidelberg.de/gaia/q3/cone/info#note-e

Fig. 5. Distance versus effective temperature curves corresponding to evolutionary sequences of DB WD models extracted from Althaus et al. (2009) with different stellar masses and the apparent magnitude V of the DBV star GD 358 (red circle with error bars), characterised by $T_{eff} = 24\,937 \pm 1018$ K and $d_{BJ} = 42.99 \pm 0.05$ pc. The uncertainty in the distance is so small that it is contained within the symbol. From linear interpolation, the astrometric mass of GD 358 is $M_{Astr} = 0.616^{+0.016}_{-0.017}\,M_\odot$.
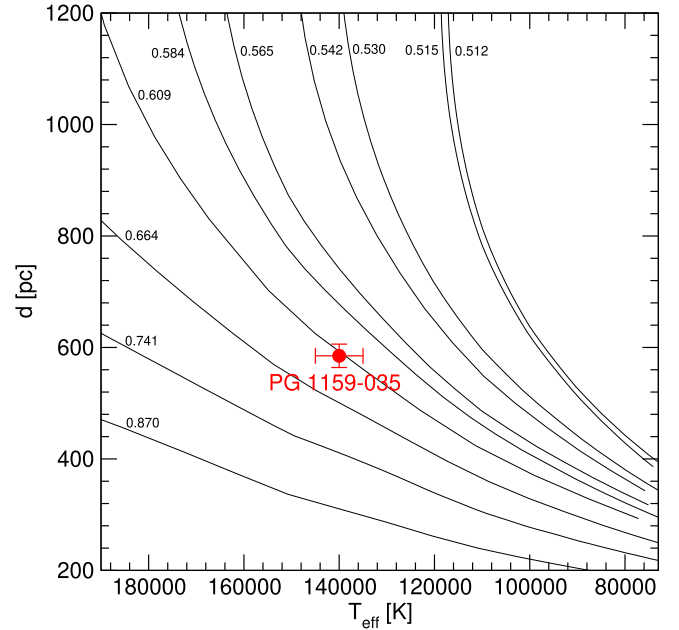
Fig. 6. Distance versus effective temperature curves corresponding to evolutionary sequences of PG 1159 models extracted from Miller Bertolami & Althaus (2006) with different stellar masses and the apparent magnitude V corresponding to the GW Vir star (DOV-type) PG 1159−035. The location of this star is marked with a red circle with error bars. The star is characterised by $T_{eff} = 140\,000 \pm 5000$ K and $d_{BJ} = 585^{+20}_{-21}$ pc. From linear interpolation, the astrometric mass of PG 1159−035 is $M_{Astr} = 0.614^{+0.028}_{-0.020}\,M_\odot$.

are contained within the symbols in Figs. 4 and 5. Consequently, the astrometric mass of these stars is primarily affected by uncertainties in T_{eff}. In contrast, GW Vir stars are much more distant, leading to more significant uncertainties in their distances. This is evident in Figs. 6 and 7. For these stars, the uncertainties in the astrometric masses arise from both T_{eff} errors and d_{BJ}. Despite these challenges, the uncertainties in astrometric masses of GW Vir stars are generally comparable to those of seismological masses, and both are notably smaller than the uncertainties associated with spectroscopic masses (refer to Table B.3 and Sect. 4.3 for further details).

3.4. Photometric masses

In the photometric method (see, e.g., Bergeron et al. 1997, 2019), the spectral energy distribution of a star is compared with model atmospheres using synthetic photometry. Magnitudes are converted to fluxes and compared with model fluxes averaged over the same filter bandpasses. The effective temperature (T_{eff}) and solid angle ($\pi(R_\star/D)^2$) are considered free parameters, and the atmospheric composition is typically assumed to be pure H or He. If the star's distance (D) is known, often from trigonometric parallax measurements, its radius ($R_\star$) can be directly obtained, allowing for the calculation of the star's mass using WD mass-radius relationships ($M_\star - R_\star$).

The combination of accurate parallaxes from *Gaia* and optical photometry (e.g. SDSS *ugriz*, Pan-STARRS *grizy*, or *Gaia*) has made the photometric method a robust tool for determining WD parameters (see, e.g., Bergeron et al. 2019; Genest-Beaulieu & Bergeron 2019a; Gentile Fusillo et al. 2019, 2021; Tremblay et al. 2019). Notably, Genest-Beaulieu & Bergeron (2019a,b) provide a

thorough comparison of the spectroscopic and photometric parameters of a large sample of DA and DB WDs.

In this work, we adopted a straightforward approach to determine the photometric mass of the DAV and DBV stars in our sample. We employed the catalogue from Gentile Fusillo et al. (2021), where T_{eff}, $\log g$, and $M_\star$ for a large selection of WDs were derived using the photometric method based on *Gaia* astrometry and photometry. To obtain the stellar radius – a parameter not tabulated in their catalogue – we combined their parameters with the same mass-radius relationships from Bédard et al. (2020) that they employed, yielding a model-independent value. Next, we applied our LPCODE WD mass-radius relationships to compute the photometric mass (M_{phot}), ensuring consistency with the other mass estimates in this study. The results are listed in the last columns of Tables B.1 and B.2. Regarding our sample of GW Vir stars, to our very best knowledge, there are no photometric mass or radius determinations. We hope that future studies will provide these determinations to complete the picture. However, the issue in this case is that these stars are exceptionally hot, resulting in an energy distribution in the optical spectrum that adheres to the Rayleigh-Jeans approximation. Consequently, this distribution becomes largely insensitive to effective temperature, as illustrated, for example, in Figure 3 of Bédard et al. (2020). Therefore, it seems unlikely that photometric parameters will be obtainable for these stars, at least not through the use of optical photometry.

4. Analysis

In this section, we assess the consistency of spectroscopic, seismological, astrometric, and photometric (although only for DAVs and DBVs) masses through comparisons. We also
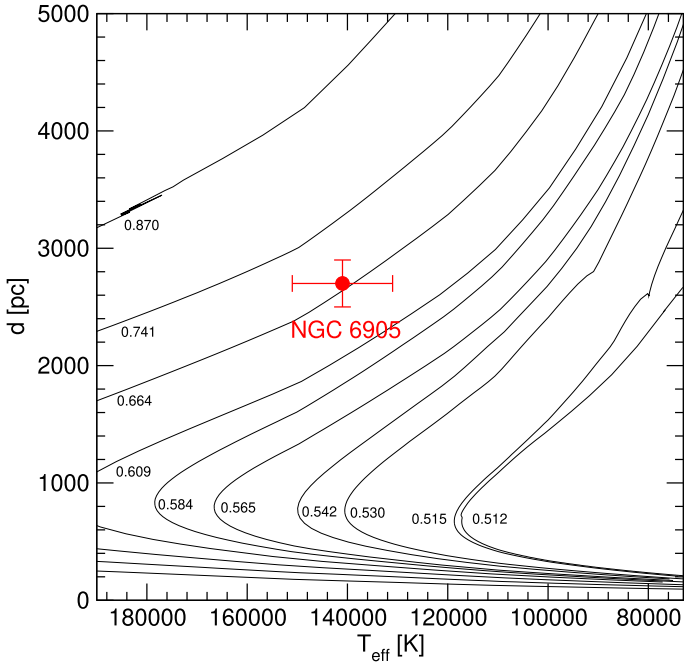
Fig. 7. Distance versus effective temperature curves corresponding to evolutionary sequences of PG1159 models extracted from Miller Bertolami & Althaus (2006) with different stellar masses and the apparent magnitude V corresponding to the GW Vir star (PNNV-type) NGC 6905 (red circle with error bars), characterised by $T_{\text{eff}} = 141\,000 \pm 10\,000$ K and $d_{\text{BJ}} = 2700 \pm 200$ pc. From linear interpolation, the astrometric mass of NGC 6905 is $M_{\text{Astr}} = 0.668^{+0.063}_{-0.044}\ M_\odot$.

examine seismological masses derived from period spacing for DBVs and GW Vir stars whenever feasible. To gauge the linear correlation between two sets of masses, we employ the Pearson coefficient r (see, for instance, Benesty et al. 2009). This coefficient ranges from -1 to $+1$, with 0 indicating that there is no linear association, and a strong correlation as r approaches 1 in absolute value. However, a high correlation does not necessarily imply a good agreement between masses, as r measures the strength of the relationship, not the agreement itself. For a more suitable assessment of the agreement, we turn to the Bland-Altman analysis (Altman & Bland 1983; Giavarina 2015). This involves plotting mass differences against their average values, helping to identify biases and outliers. The agreement limits are defined as $\pm 1.96\sigma$, where σ represents the standard deviation of the differences. In our analysis, we adopt a stricter criterion, using $\pm 1\sigma$ to define agreement limits, enabling the identification of outlier WD stars with significantly different masses derived from various methods.

4.1. DAV stars

We compare M_{Spec} and M_{Seis}, M_{Seis} and M_{Astr}, M_{Spec} and M_{Astr}, M_{Phot} and M_{Astr}, M_{Seis} and M_{Phot}, and M_{Spec} and M_{Phot} for DAV stars in Figs. 8 to 13. Upon inspection of the figures, significant agreement is observed among the different sets of masses, particularly for masses below $\sim 0.75\ M_\odot$, a trend that becomes apparent upon examination of the Pearson linear correlation coefficient. It is evident that in all cases this coefficient exceeds $\sim +0.8$, indicating a strong correlation. However, we are also interested in knowing how closely the sets of mass values agree, discovering whether there are global biases or not, and find-
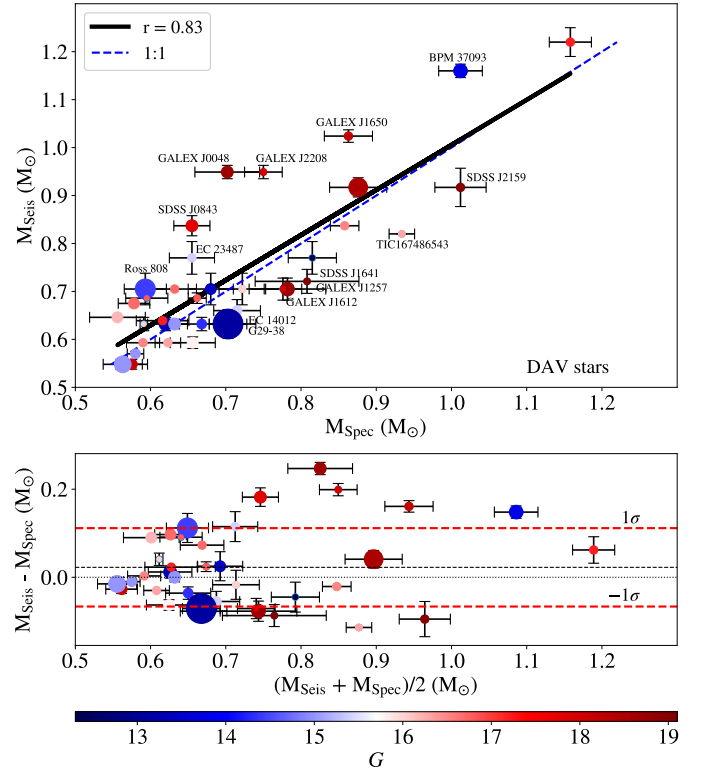

Fig. 8. Comparison of stellar masses for DAV stars. Upper panel: Dispersion diagram showing the comparison between the spectroscopic and the seismological masses for DAVs (see Table B.1). The blue dashed line indicates the 1:1 correspondence between the two sets of stellar masses. The labeled stars correspond to the cases where the mass estimates exhibit substantial discrepancies. The thick black line indicates the Pearson correlation fit. Lower panel: Bland-Altman diagram showing the mass difference in terms of the average mass for each object. The black short-dashed line corresponds to the mean difference, $\langle \Delta M_\star \rangle$, whereas the two red dashed lines represent the limits of agreement, $\langle \Delta M_\star \rangle$, considering the deviation of $\pm 1\sigma$. In both panels, the size of each symbol is proportional to the number of g-mode pulsation periods used to derive the seismological model (fourth column of Table B.1), and the colour palette indicates the apparent magnitude *Gaia G* (fifth column of Table A.1) of each star.

ing outlier stars whose masses should be re-evaluated in future analyses.

We first start by comparing the stellar masses of DAVs obtained from spectroscopy and those corresponding to seismological models in a dispersion diagram, as shown in the upper panel of Fig. 8. In the figure, the blue dashed line represents the 1:1 line of correspondence between the two sets of stellar mass values. Stars whose mass estimates exhibit substantial discrepancies (i.e. deviate noticeably from the 1:1 line of correspondence) are labeled with their respective names. The Pearson coefficient, which measures the correlation between M_{Spec} and M_{Seis} in this case is $r = +0.83$, revealing a strong correlation. M_{Spec} and M_{Seis} show good agreement, which is somewhat anticipated, as seismological models are typically selected to satisfy the spectroscopic constraints of T_{eff} and $\log g$. This selection is made to mitigate the intrinsic degeneracy of solutions often encountered as a result of period-to-period fits (see, for instance, Romero et al. 2012, 2013). However, there are significant discrepancies for some stars more massive than $\sim 0.75\ M_\odot$, as evidenced by their deviation from the 1:1 line of correspondence. The lower panel of the figure depicts the Bland-Altman
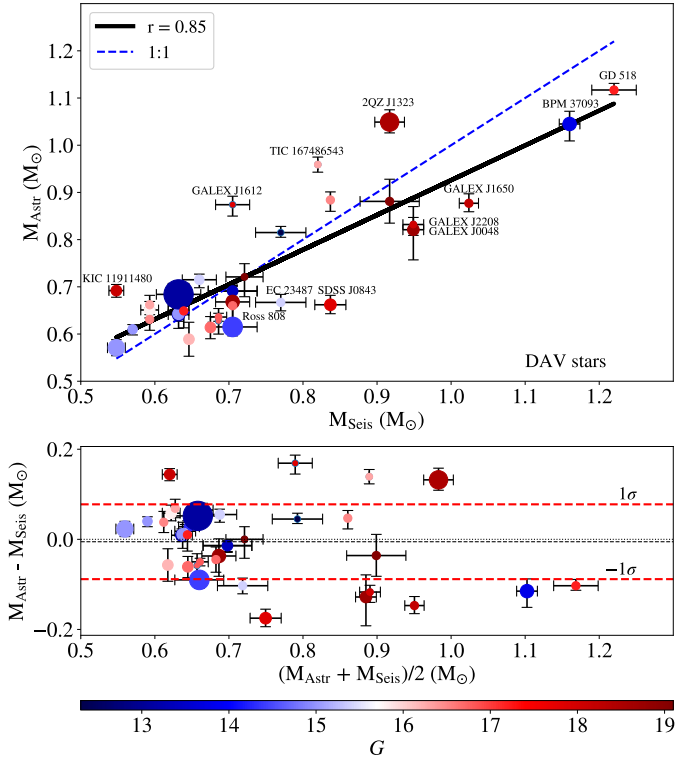
Fig. 9. Similar to Fig. 8 but for the comparison between seismological and astrometric masses.

Fig. 10. Similar to Fig. 8 but for the comparison between spectroscopic and astrometric masses.

diagram, where the mass differences, $\Delta M_\star = M_{\mathrm{Seis}} - M_{\mathrm{Spec}}$, are plotted against the mean mass value, $\langle M_\star \rangle = (M_{\mathrm{Seis}} + M_{\mathrm{Spec}})/2$, for each star. The mean difference is $\langle \Delta M_\star \rangle = 0.023$, indicating a small positive bias represented by the gap between the x axis (corresponding to zero differences, marked by the dotted line) and the short-dashed line parallel to the x axis at 0.023 units. This suggests that on average, the seismological masses are somewhat higher than the spectroscopic ones. The limits of agreement, defined as the $\pm 1\sigma$ departure from the mean difference, are displayed with red dashed lines at $\langle \Delta M_\star \rangle \pm 0.089\, M_\odot$. From this diagram, it is clear that there are outlier stars for which the mass difference is beyond the agreement limits, in accordance with what the dispersion diagram (upper panel) indicates. In these diagrams, the size of the symbols is directly proportional to the number of periods used to obtain the seismological models (fourth column of Table B.1), while the colour of each symbol is related to the brightness of the star (the apparent *Gaia* magnitude G in the bottom palette of colours). Clearly, most outlier stars are dim (high G value). One exception is BPM 37093, which is bright but nonetheless exhibits a large mass discrepancy. Furthermore, there is no clear indication that the number of periods is crucial for the star to have discrepant spectroscopic and seismological masses.

The comparison between seismological and astrometric masses (upper panel of Fig. 9) closely resembles the situation analysed above for spectroscopic and seismological masses (Fig. 8). It is evident that there is strong agreement between M_{Seis} and M_{Astr}, particularly for $M_\star \lesssim 0.75\, M_\odot$. However, discrepancies become more apparent for larger masses, with data points deviating further from the 1:1 identity line. The Pearson coefficient for this comparison is $r = +0.86$, indicating a robust correlation. In the Bland-Altman diagram (lower panel of Fig. 9), we observe a small negative mean mass difference of
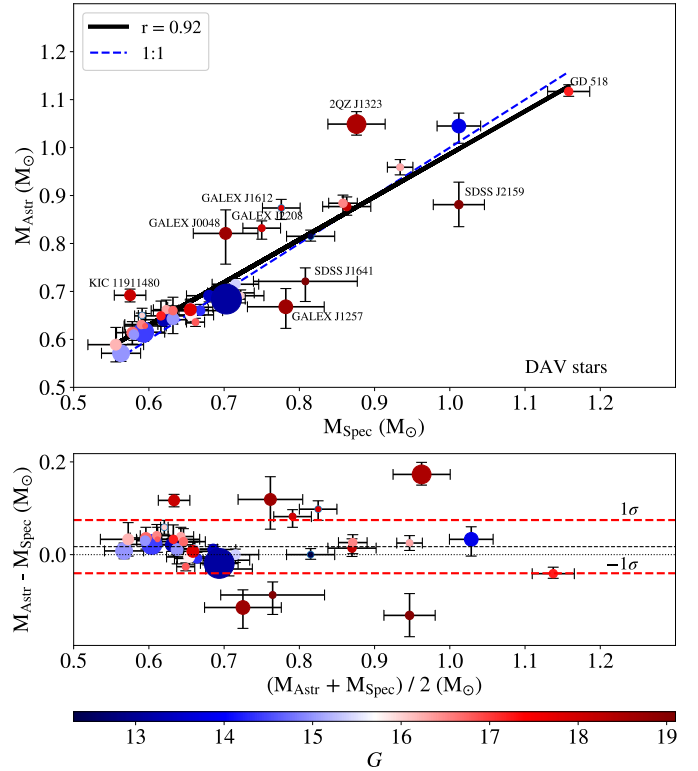
$\langle \Delta M_\star \rangle = \langle M_{\mathrm{Astr}} - M_{\mathrm{Seis}} \rangle = -0.005\, M_\odot$, suggesting a slight negative bias between M_{Seis} and M_{Astr} masses (with M_{Seis} tending to be slightly larger than M_{Astr} on average). The limits of agreement, $\langle \Delta M_\star \rangle \pm 0.083\, M_\odot$, are very similar to those observed in the comparison between spectroscopic and seismological masses (Fig. 8). Once again, BPM 37093 stands out among outliers, exhibiting a significant discrepancy between seismological and astrometric masses despite being a bright object.

When comparing spectroscopic masses with astrometric masses, a very strong correlation is observed ($r = 0.92$, upper panel of Fig. 10). In particular, we can see a very dense crowding of points close to the 1:1 correspondence line for objects with masses less than $\sim 0.75\, M_\odot$, while there are several more massive objects that deviate from the line of identity, reflecting considerable discrepancies in the value of the stellar mass depending on the method used to derive it. In the corresponding Bland-Altman diagram (lower panel), a slight bias towards larger astrometric masses than spectroscopic ones is observed, with a positive mean difference of $\langle \Delta M_\star \rangle = \langle M_{\mathrm{Astr}} - M_{\mathrm{Spec}} \rangle = +0.017\, M_\odot$. The limits of agreement, $\langle \Delta M_\star \rangle \pm 0.057\, M_\odot$, suggest that the mass differences are less scattered compared to the previous analyses. Notably, all outlier stars in this case are dim.

Upon analysing the relationship between photometric and astrometric masses shown in Fig. 11, we find a very strong correlation, as indicated by the $r = +0.93$ value in the upper panel. M_{Phot} and M_{Astr} show a significant agreement, in general, which is not surprising given that, although determined through very different procedures, the two methods employ photometry and astrometry from *Gaia*. The agreement between photometric and astrometric masses is particularly true for stars with $M_\star \lesssim 0.75\, M_\odot$, while for some more massive stars, a deviation from the 1:1 line of correspondence is found. The Bland-Altman diagram (lower panel) reveals a positive mean mass difference of
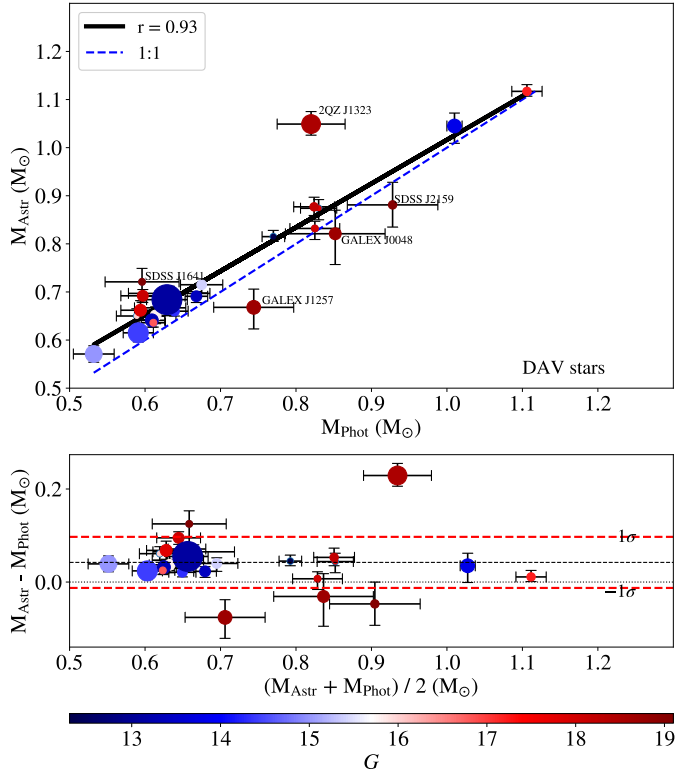
Fig. 11. Similar to Fig. 8 but for the comparison between photometric and astrometric masses.

Fig. 12. Similar to Fig. 8 but for the comparison between seismological and photometric masses.

$\langle \Delta M_\star \rangle = \langle M_{\mathrm{Astr}} - M_{\mathrm{Phot}} \rangle = +0.042 \, M_\odot$, indicating a noticeable bias where astrometric masses exceed photometric masses. The limits of agreement, $\langle \Delta M_\star \rangle \pm 0.055 \, M_\odot$, similarly to the previous case, are also less scattered than the first two cases (M_{Spec} vs. M_{Seis} and M_{Seis} vs. M_{Astr}). We also note that all the outlier stars in this case are dim.

In assessing the comparison between seismological and photometric masses, we find a similar dispersion diagram (upper panel in Fig. 12) as the one shown in the comparison between astrometric and seismological masses. In this case, $r = +0.88$, indicating again a strong correlation. It is clear that there is close agreement between the seismological and photometric masses, although some discrepancies are found, particularly for stars between, roughly, 0.7 and 1 $M_\odot$. In the Bland-Altman diagram (lower panel in Fig. 12), there is a negative mean mass difference of $\langle \Delta M_\star \rangle = \langle M_{\mathrm{Phot}} - M_{\mathrm{Seis}} \rangle = -0.055 \, M_\odot$, indicating that photometric masses are, on average, larger than seismological masses. The limits of agreement, $\langle \Delta M_\star \rangle \pm 0.083 \, M_\odot$ are also very similar to those found in the comparison between astrometric and seismological masses. In this case, as before, we once again find BPM 37093 as an outlier star.

Finally, when comparing spectroscopic and photometric masses, illustrated in Fig. 13, we observe a strong correlation as reflected by the $r = +0.90$ value shown in the upper panel. The Bland-Altman diagram (lower panel) indicates that there is a negative mean mass difference of $\langle \Delta M_\star \rangle = \langle M_{\mathrm{Phot}} - M_{\mathrm{Spec}} \rangle = -0.031 \, M_\odot$, implying that photometric masses are generally lower than spectroscopic masses. In this case, the limits of agreement are $\langle \Delta M_\star \rangle \pm 0.063 \, M_\odot$, and it is clear that all outlier stars are dim.

In summary, the masses of DAV stars derived from the four methods considered generally show good agreement, particularly for masses below approximately 0.75 $M_\odot$. How-
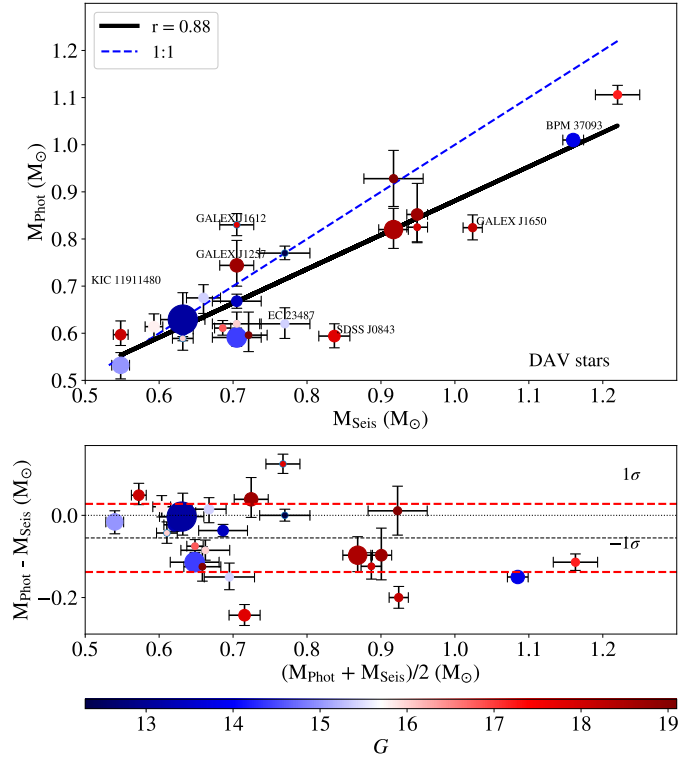
ever, there are notable discrepancies for certain DAV stars. Table B.4 lists the objects classified as outliers, where there are discrepancies between the mass values derived from different methods. An outlier is identified when $\langle M_\star \rangle - \sigma \geq \Delta M_\star \geq \langle M_\star \rangle + \sigma$. For outlier DAV stars BPM 37093, GALEX J1650+3010, GALEX J2208+0654, GALEX J0048+1521, SDSS J0843+0431, and EC 23487−2424, we observe $M_{\mathrm{Seis}} > M_{\mathrm{Astr}} \gtrsim M_{\mathrm{Spec}}$. This suggests that spectroscopic masses for these stars might be slightly underestimated, while seismological masses could be overestimated and require reassessment. Regarding BPM 37093, we note that the mass of this star would vary slightly if we were to use CO-core WD models. However, the seismological analysis of this star was performed using ONe core WD models (Córsico et al. 2019b). Therefore, for consistency, we used ONe-core WD evolutionary tracks in this paper to derive both spectroscopic and astrometric masses. It is interesting to note that the photometric mass of this star is very similar to the spectroscopic mass. Conversely, for SDSS J2159+1322 and GALEX J1257+0124, we find $M_{\mathrm{Spec}} > M_{\mathrm{Phot}} \gtrsim M_{\mathrm{Seis}} \gtrsim M_{\mathrm{Astr}}$, which indicates the potential overestimation of spectroscopic masses. TIC 167486543 and GALEX J1612+0830 exhibit $M_{\mathrm{Astr}} > M_{\mathrm{Spec}} > M_{\mathrm{Seis}}$, suggesting that both seismological and spectroscopic masses might be underestimated. Similarly, for the pair 2QZ J1323+0103 and KIC 11911480, we observe $M_{\mathrm{Astr}} > M_{\mathrm{Seis}} \gtrsim M_{\mathrm{Spec}}$, indicating the potential underestimation of both seismological and spectroscopic masses. The case of Ross 808 shows $M_{\mathrm{Seis}} > M_{\mathrm{Astr}} \simeq M_{\mathrm{Spec}} \simeq M_{\mathrm{Phot}}$, suggesting a possible overestimation of the seismological mass. Finally, for SDSS J1641+3521, we find $M_{\mathrm{Spec}} > M_{\mathrm{Seis}} = M_{\mathrm{Astr}} > M_{\mathrm{Phot}}$, indicating a potential overestimation of spectroscopic mass, necessitating a review of T_{eff} and $\log g$, and a potential underestimation of photometric mass.
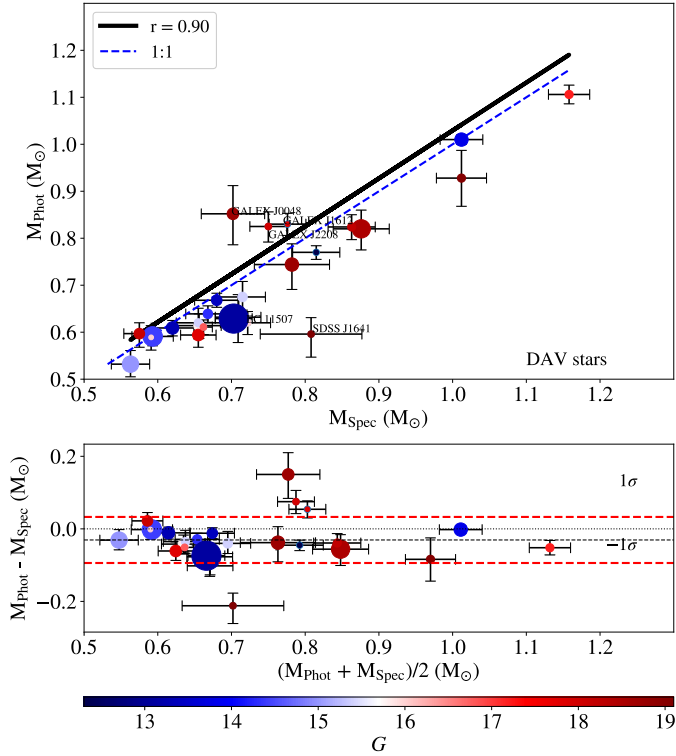
Fig. 13. Similar to Fig. 8 but for the comparison between spectroscopic and photometric masses.

Fig. 14. Comparison of stellar masses for DBV stars. Upper panel: Dispersion diagram displaying the comparison between the spectroscopic and asteroseismological masses for DBVs (see Table B.2). All the stars are identified by their names. Bottom panel: Corresponding Bland-Pearson diagram. The meaning of the different lines in both panels is the same as in Fig. 8.

4.2. DBV stars

We present comparisons between $M_{\rm Spec}$ and $M_{\rm Seis}$, $M_{\rm Spec}$ and $M_{\rm Seis}(\Delta\Pi)$, $M_{\rm Seis}$ and $M_{\rm Astr}$, $M_{\rm Spec}$ and $M_{\rm Astr}$, $M_{\rm Spec}$ and $M_{\rm Phot}$, $M_{\rm Phot}$ and $M_{\rm Astr}$, $M_{\rm Seis}$ and $M_{\rm Phot}$, and $M_{\rm Phot}$ and $M_{\rm Seis(\Delta\Pi)}$ for DBVs in Figs. 14 to 21. $M_{\rm Seis}(\Delta\Pi)$ represents the seismological stellar mass derived on the basis of uniform period spacing. Among these figures, we observe two different levels of correlation. Five out of eight (Figures 14 to 18, displaying $M_{\rm Spec}$ and $M_{\rm Seis}$, $M_{\rm Spec}$ and $M_{\rm Seis}(\Delta\Pi)$, $M_{\rm Seis}$ and $M_{\rm Astr}$, $M_{\rm Spec}$ and $M_{\rm Astr}$, and $M_{\rm Spec}$ and $M_{\rm Phot}$) indicate a moderate linear correlation, with Pearson coefficients that do not exceed $\sim +0.66$, while the remaining three (Figures 19 to 21, showing $M_{\rm Phot}$ and $M_{\rm Astr}$, $M_{\rm Seis}$ and $M_{\rm Phot}$, and $M_{\rm Phot}$ and $M_{\rm Seis(\Delta\Pi)}$) exhibit a stronger correlation, with Pearson coefficients that range from $+0.77$ to $+0.92$. Notably, of the four figures that involve comparisons with photometric masses, three of them are the ones showing a higher degree of correlation. This suggests a potential trend where comparisons involving photometric masses tend to exhibit a stronger correlation.

We first turn our attention to the cases with moderate correlation (Figures 14 to 18). The Bland-Pearson diagrams reveal significant biases among the methods of stellar mass derivation, indicating poor agreement among the various mass sets. Identifying outlier stars based on agreement limits becomes a challenge. In cases where there is a notable bias between the two mass sets, characterised by a mean difference considerably different from zero, a star may fall within admissibility limits because its distance from the mean difference, $\langle\Delta M_\star\rangle$, is within $\pm\sigma$. However, it could still be located far from the 1:1 correspondence line, indicating significant mass discrepancies. Conversely, an object may appear close to the 1:1 correspondence line, suggesting good mass agreement, but fall outside admissi-
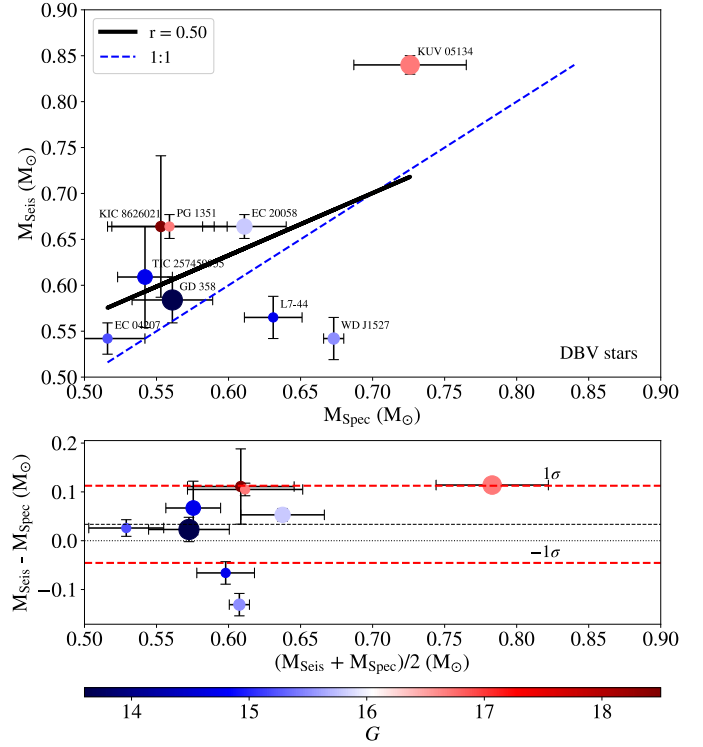
bility limits in the Bland-Altman diagram, leading to erroneous outlier classification.

Notably, a consistent trend is observed in most comparisons: spectroscopic masses are systematically smaller than seismological and astrometric masses. For example, in Fig. 14, where seismological masses are compared with spectroscopic masses, seven out of nine DBV stars exhibit spectroscopic masses smaller than seismological masses. This trend is evident in the mean mass difference of $\langle\Delta M_\star\rangle = 0.034\,M_\odot$, indicating a notable bias towards seismological masses being greater than spectroscopic masses. It is important to note that the limits of agreement, $\langle\Delta M_\star\rangle \pm 0.079\,M_\odot$, prove to be inappropriate to identify outliers. In fact, KUV 05134+2605, KIC 8626021, and PG 1351+489 clearly stand out as outliers, positioned significantly away from the 1:1 correspondence line, despite falling at the upper limit of agreement. TIC 257459955 is also evidently an outlier, despite falling within the agreement limits.

The discrepancy between different sets of masses becomes more apparent when comparing spectroscopic masses with seismological masses derived from period spacing (Fig. 15). In this comparison, seven out of nine stars exhibit spectroscopic masses smaller than their seismological counterparts. It is important to note that for two stars (PG 1351+489 and EC 20058−5234), the seismological mass is defined within a range of values (see Table B.2), where we have taken the average value of both extremes as the seismological mass. The bias towards larger seismological masses compared to spectroscopic ones is more pronounced here, with an average mass difference of $\langle\Delta M_\star\rangle = 0.085\,M_\odot$. Unfortunately, the Bland-Altman diagram does not effectively identify outliers. For instance, despite
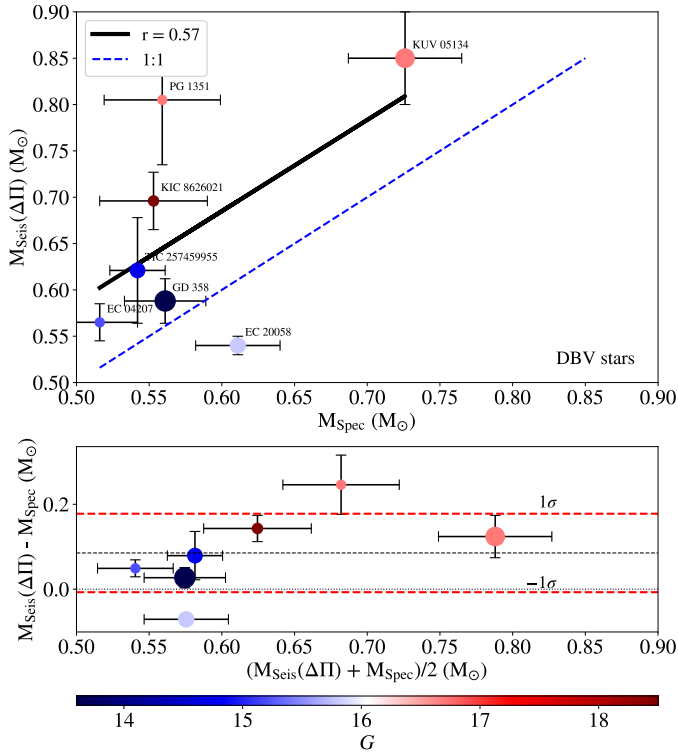
Fig. 15. Similar to Fig. 14, this figure illustrates the comparison between spectroscopic and seismological masses, with the seismological mass derived from the period spacing ($\Delta\Pi$). It is worth noting that only seven out of the total nine DBV stars analysed have an estimate of seismological mass from the period spacing (see Table B.2).

Fig. 16. Similar to Fig. 14 but for the comparison between the seismological and astrometric masses.

Fig. 17. Similar to Fig. 14 but for the comparison between spectroscopic and astrometric masses.

KUV 05134+2605 and KIC 8626021 being outliers according to the scatter plot, they fall well within the limits of agreement in the Bland-Altman diagram.

In the comparison between seismological and astrometric masses (Fig. 16), it is clear that astrometric masses generally exceed seismological masses, with an average mass difference of $\langle \Delta M_\star \rangle = 0.045\,M_\odot$. Furthermore, when comparing spectroscopic masses with astrometric masses (Fig. 17), it is noteworthy that all spectroscopic masses are below the astrometric masses. Here, the average mass difference amounts to $\langle \Delta M_\star \rangle = 0.079\,M_\odot$. In fact, spectroscopic masses are approximately 14% smaller than astrometric masses on average. Validating this trend would require analysing a broader sample of DB WD stars, a task planned for a future paper.

The observed trend of spectroscopic masses being systematically smaller than the other mass estimates does not hold, however, when comparing them to photometric masses, as shown in Fig. 18. Indeed, we find a slight bias towards larger photometric masses, reflected in the mean mass difference $\langle \Delta M_\star \rangle = 0.013\,M_\odot$. The lower panel reveals that the limits of agreement, $\langle \Delta M_\star \rangle \pm 0.065\,M_\odot$, are once again inadequate for identifying outliers. This is evident from L7−44 and EC 20058−5234, which, despite being clear outliers in the upper panel, fall within or almost exactly on the limits of agreement in the lower panel.

Now we focus on the cases exhibiting strong correlations, specifically between M_Phot and M_Astr, M_Phot and $M_\mathrm{Seis}(\Delta\Pi)$, and M_Seis and M_Phot. In the first case, where we compare photometric and astrometric masses, as illustrated in Fig. 19, the Pearson coefficient is high, $r = +0.92$. The upper panel clearly shows that all astrometric masses surpass the photometric ones, similar to what is found in the comparison between spectro-

scopic and astrometric masses. Here, the mean mass difference is $\langle \Delta M_\star \rangle = 0.045\,M_\odot$, and we find that astrometric masses are approximately 11% greater than their photometric counterparts. Confirming this trend between astrometric and photometric
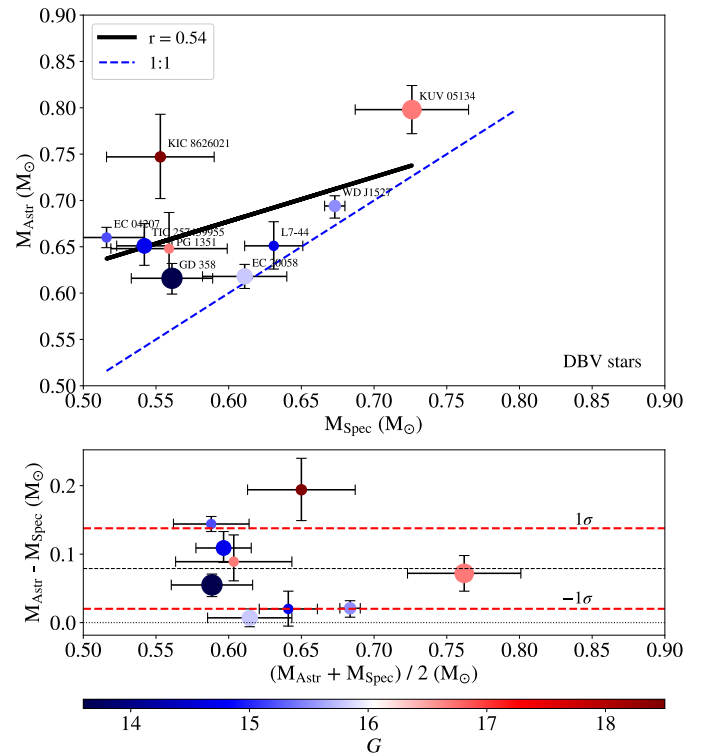
Fig. 18. Similar to Fig. 14 but for the comparison between spectroscopic and photometric masses.
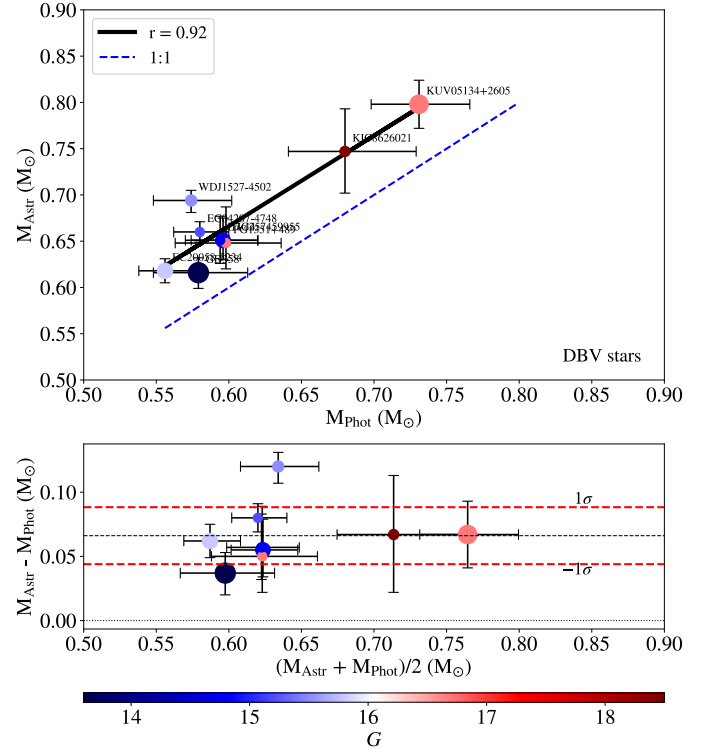
Fig. 19. Similar to Fig. 14 but for the comparison between photometric and astrometric masses.

masses will necessitate further analysis with a larger sample of DB WDs, as already mentioned and planned for future work.

When comparing seismological and photometric masses, a strong correlation is evident, with a Pearson coefficient of $r = +0.80$, as shown in the upper panel of Fig. 20. This is particularly true for stars with masses $\lesssim 0.6\,M_\odot$. In the lower panel, the mean mass difference of $\langle \Delta M_\star \rangle = -0.021\,M_\odot$ indicates that seismological masses slightly exceed photometric ones. Lastly, Fig. 21 presents the comparison between $M_{\rm Phot}$ and $M_{\rm Seis}(\Delta\Pi)$. The correlation in this case is $r = +0.77$, slightly lower than in the previous case. However, it remains evident that objects with masses $\lesssim 0.6\,M_\odot$ are close to the 1:1 correspondence line. The mean mass difference of $\langle \Delta M_\star \rangle = 0.031\,M_\odot$ indicates a tendency for seismological masses derived from the period spacing to be slightly larger than photometric ones.

In the following, we delve into describing the significant discrepancies observed in some of the DBV stars. We provide below a detailed analysis of cases where notable disagreements arise.

– KUV 05134+2605: With an extensive dataset of 16 detected periods, but not being very bright ($G = 16.749$), this star exhibits the trend $M_{\rm Seis} \simeq M_{\rm Seis}(\Delta\Pi) > M_{\rm Astr} \gtrsim M_{\rm Phot} \simeq M_{\rm Spec}$. The masses derived from asteroseismology ($M_{\rm Seis}, M_{\rm Seis}(\Delta\Pi)$) appear notably high among the other estimates, in clear contrast to the low value of the spectroscopic mass ($M_{\rm Spec}$). Given the close agreement between $M_{\rm Phot}$, $M_{\rm Spec}$, and $M_{\rm Astr}$, our results might suggest that the higher masses obtained from asteroseismology warrant a reevaluation.

– KIC 8626021: Here, we observe $M_{\rm Astr} > M_{\rm Seis}(\Delta\Pi) \simeq M_{\rm Phot} \simeq M_{\rm Seis} > M_{\rm Spec}$. This star, with a faint brightness ($G = 18.500$) and a limited number of periods (5), exhibits a notably small spectroscopic mass, highlighting the need for

a thorough revision of the spectroscopic parameters ($T_{\rm eff}$ and $\log g$).

– PG 1351+489: In this case, we find $M_{\rm Seis}(\Delta\Pi) > M_{\rm Seis} \simeq M_{\rm Astr} > M_{\rm Phot} > M_{\rm Spec}$. The seismological mass derived
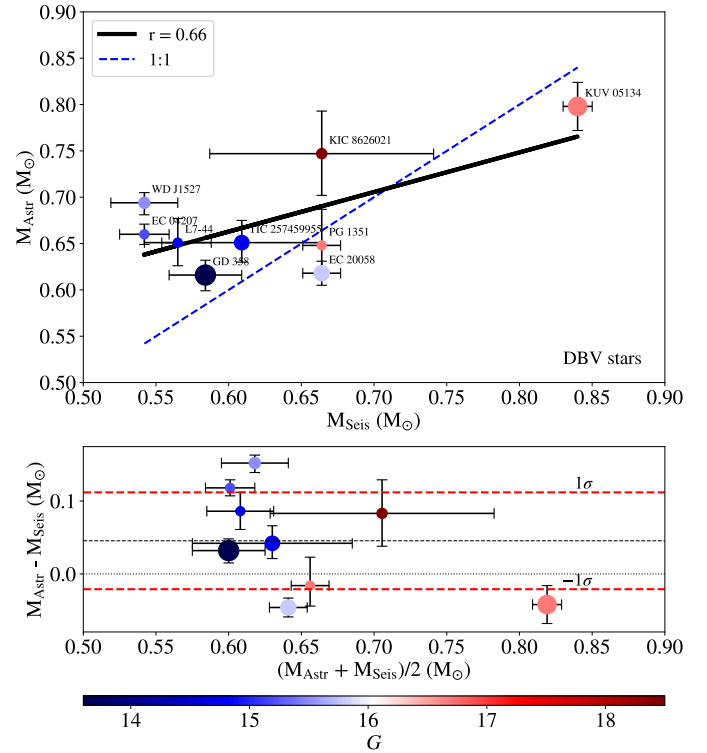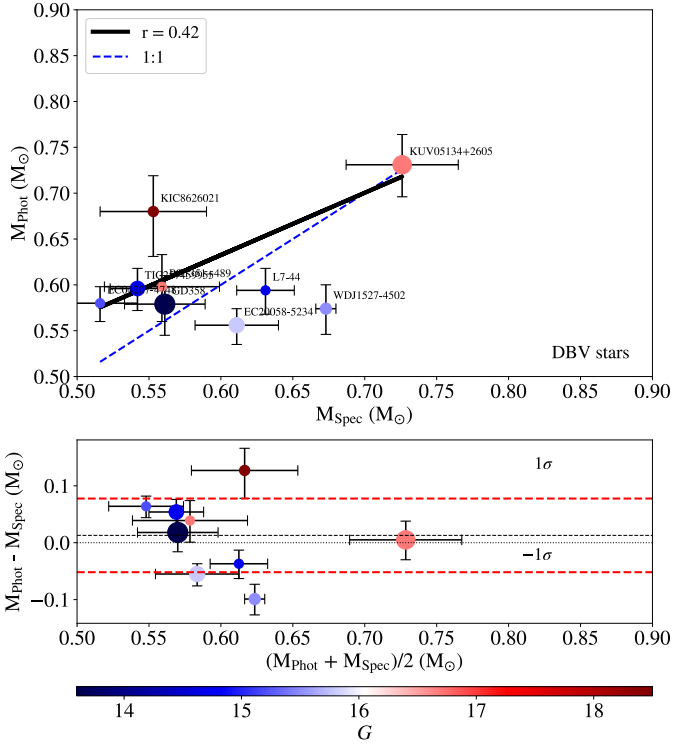

Fig. 20. Similar to Fig. 14 but for the comparison between seismological and photometric masses.

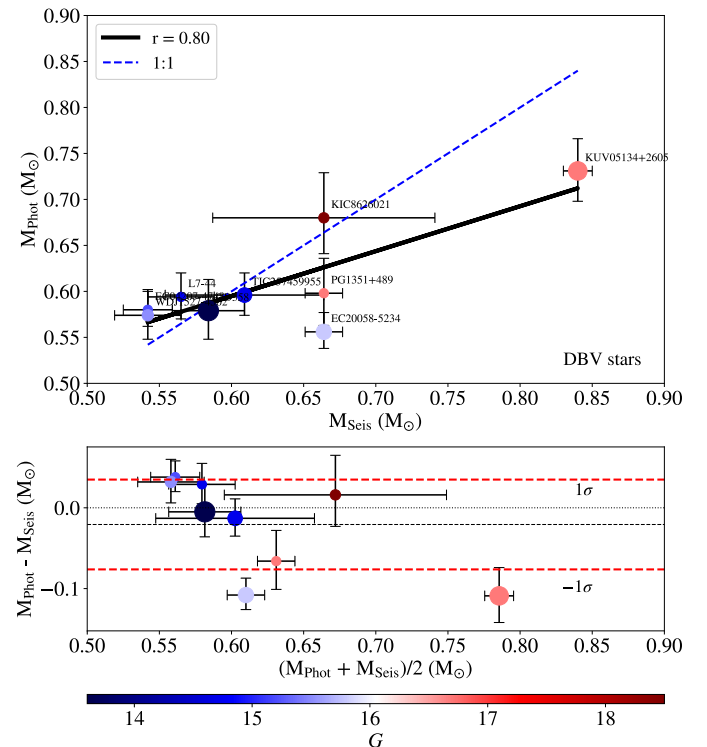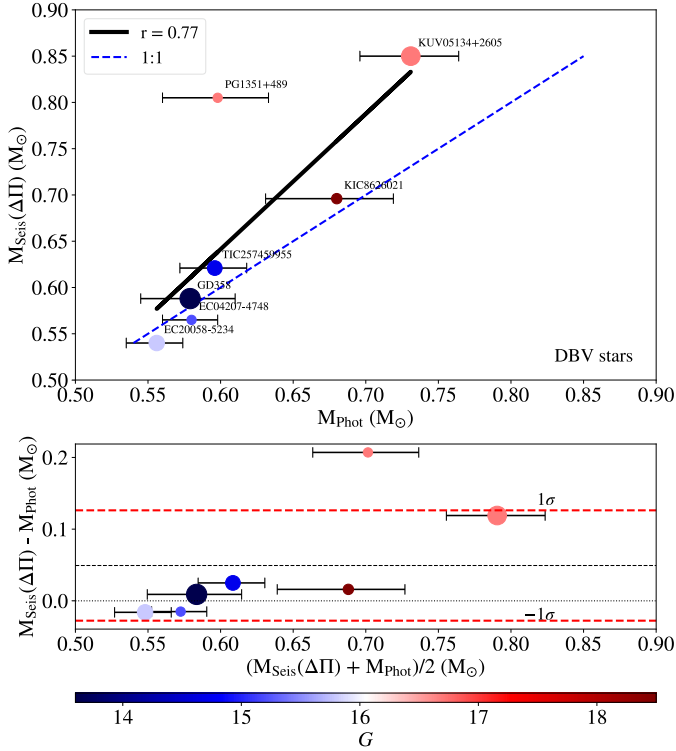**Fig. 21.** Similar to Fig. 15 but for the comparison between photometric and seismological masses derived from the period spacing.

from the period spacing appears to be notably high ($0.740 \lesssim M_\star/M_\odot \lesssim 0.870$). In contrast, the spectroscopic mass is markedly low, indicating a need for refinement to determine $T_{\rm eff}$ and $\log g$.

- WD J1527−4502: For this star, we get $M_{\rm Astr} \gtrsim M_{\rm Spec} > M_{\rm Phot} > M_{\rm Seis}$, suggesting that the spectroscopic mass is well determined, but the seismological mass is low in excess. The photometric mass is also lower compared to $M_{\rm Astr}$ and $M_{\rm Spec}$, but to a lesser extent than the seismological mass. For this star, there is no assessment of the seismological mass based on the period spacing. Our results suggest a review of the seismological mass of WD J1527−4502.

It is worth highlighting that, beyond these four troublesome stars, the remaining DBV stars in the small sample show varying degrees of inconsistency in their mass values depending on the method used. Below, we describe each one of these cases:

- EC 20058−5234: In this case, we observe $M_{\rm Seis} > M_{\rm Spec} \simeq M_{\rm Astr} > M_{\rm Phot} \simeq M_{\rm Seis}(\Delta\Pi)$. This suggests the reliability of the spectroscopic mass, which aligns with the astrometric mass. However, the seismological mass derived from individual periods appears to be overstated. Interestingly, the photometric mass aligns well with the seismological mass based on period spacing, although both of these are lower compared with the spectroscopic and astrometric values. Consequently, a reassessment of the seismological determinations of EC20058−5234's mass seems warranted.
- TIC 257459955: In this case, $M_{\rm Astr} \simeq M_{\rm Seis}(\Delta\Pi) \simeq M_{\rm Seis} \simeq M_{\rm Phot} > M_{\rm Spec}$, indicating a notably low spectroscopic mass. Therefore, a reevaluation of the parameters $T_{\rm eff}$ and $\log g$, utilised to derive the spectroscopic mass, appears to be necessary.
- EC 04207−4748: Here, $M_{\rm Astr} > M_{\rm Phot} \simeq M_{\rm Seis} \simeq M_{\rm Seis}(\Delta\Pi) > M_{\rm Spec}$. This suggests an underestimation of the

spectroscopic mass, implying a need for a reassessment of the spectroscopic parameters for this star.

- L 7−44: Here, we find $M_{\rm Astr} \gtrsim M_{\rm Spec} > M_{\rm Phot} > M_{\rm Seis}$, suggesting an underestimation of the seismological mass, which warrants a re-assessment.
- GD 358: As the prototype of DBV stars (also known as V777 Her stars), we observe $M_{\rm Astr} \gtrsim M_{\rm Seis} \simeq M_{\rm Seis}(\Delta\Pi) \simeq M_{\rm Phot} > M_{\rm Spec}$. These findings imply a possible underestimation of the spectroscopic mass of GD 358. Therefore, it is advisable to reevaluate the spectroscopic parameters ($T_{\rm eff}$ and $\log g$) utilised to calculate $M_{\rm Spec}$.

We conclude our analysis of the DBV stars by highlighting a trend that is consistent across most cases: the spectroscopic mass values appear to be systematically underestimated. This observation raises the possibility of encountering challenges in precisely determining $T_{\rm eff}$ and $\log g$ through spectroscopic methods for DBV stars (see Sect. 5). Similar to DAVs, we do not observe a direct correlation between the reliability of seismological mass determination and either the star's brightness or the number of periods used in determining the seismological mass.

4.3. GW Vir stars

In this section, we present comparisons between $M_{\rm Spec}$ and $M_{\rm Seis}$, $M_{\rm Spec}$ and $M_{\rm Seis}(\Delta\Pi)$, $M_{\rm Seis}$ and $M_{\rm Astr}$, and $M_{\rm Spec}$ and $M_{\rm Astr}$ for GW Vir stars in Figures 22, 23, 24, and 25, respectively. As we established before, for this class of pulsating stars we do not have available photometric radii or masses, which prevents us from considering comparisons with $M_{\rm Phot}$.

Let us begin by examining the comparison between the spectroscopic and seismological masses of GW Vir stars. From the upper panel of Fig. 22, it is evident that there is generally good agreement between the two sets of masses, as indicated by their proximity to the 1:1 identity line. However, certain stars exhibit significant discrepancies. For example, the seismological masses are significantly larger (by approximately 20%) than the spectroscopic masses for NGC 2371 and HS 2324+3944, while for others, such as RX J2117+3412 and NGC 246, the spectroscopic mass exceeds the seismological mass by approximately 30%. In this case, the Pearson coefficient is small and negative ($r = -0.15$), suggesting a weak and meaningless anticorrelation between the two sets of masses. Pearson's linear correlation analysis loses meaning in this case. On the other hand, the Bland-Altman diagram (bottom panel) illustrates that most stars cluster near the mean value of the mass differences, which is very small ($\langle \Delta M_\star \rangle = 0.013\,M_\odot$). This indicates a negligible bias between the two mass sets, with only four outlier stars deviating beyond the limits of agreement ($\langle \Delta M_\star \rangle \pm 0.087\,M_\odot$). These outliers include RX J2117+2117 and NGC 246 (where $M_{\rm Spec} > M_{\rm Seis}$), and HS 2324+3944 and NGC 2371 (where $M_{\rm Spec} < M_{\rm Seis}$).

Something completely analogous happens when comparing the spectroscopic masses with the seismological masses derived from the period spacing (Fig. 23). Once again, significant disparities are evident between the spectroscopic and seismological masses of the same stars NGC 2371, HS 2324+3944, RX J2117+3412, and NGC 246. In this case, the Pearson coefficient is $r = -0.25$, indicating a weak anticorrelation between $M_{\rm Seis}(\Delta\Pi)$ and $M_{\rm Spec}$. A feature worth highlighting is that the uncertainties of the spectroscopic masses are by far greater than the seismological ones. This is due to the enormous uncertainties in the spectroscopic parameters of GW Vir stars, in particular in surface gravity (see Table A.3). This is a clear symptom of the
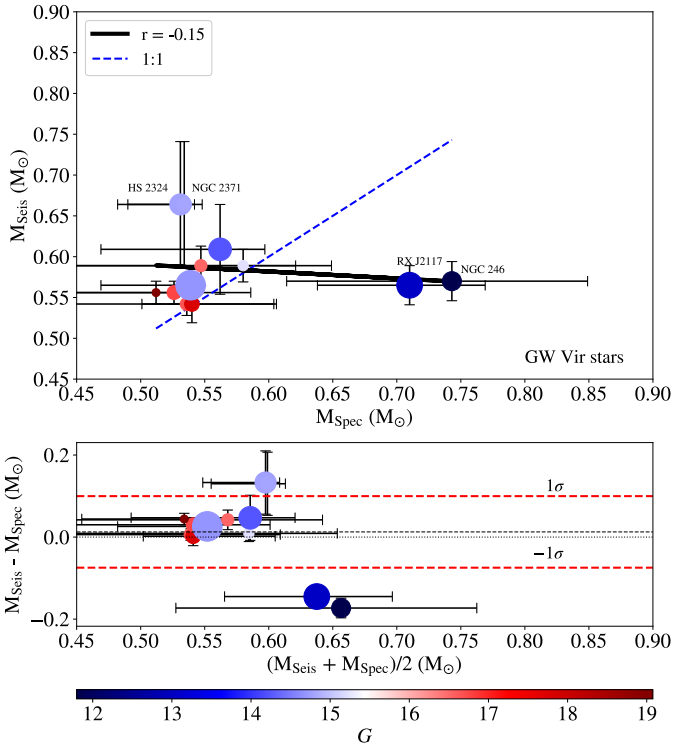
Fig. 22. Comparison of stellar masses for GW Vir stars. Upper panel: dispersion diagram showing the comparison between the spectroscopic and asteroseismological masses for GW Vir stars (refer to Table B.3). Stars with mass estimates that significantly disagree are annotated with their names. Bottom panel: corresponding Bland-Pearson diagram. The meaning of the different lines in both panels is the same as in Fig. 8.

Fig. 23. Similar to Fig. 22, this figure presents the comparison between spectroscopic and seismological masses, where the seismological masses are derived from the period spacing ($\Delta\Pi$).

difficulty in modelling the atmospheres of these extremely hot stars (see Sect. 5).

The comparison between seismological and astrometric masses of GW Vir stars is depicted in Fig. 24. Here, the Pearson coefficient is extremely small ($r = -0.01$), indicating a negligible correlation between $M_{\rm Seis}$ and $M_{\rm Astr}$. The Bland-Altman diagram reveals an almost negligible bias between the seismological and astrometric masses, with an average difference of $\langle \Delta M_\star \rangle = 0.0004\,M_\odot$. This suggests a very close agreement between both methods for deriving the masses of GW Vir stars on average. Moreover, the diagram highlights the presence of some outliers, whose mass differences exceed the agreement limits. These limits, set at $\langle \Delta M_\star \rangle \pm 0.085\,M_\odot$, are surpassed by SDSS J0754+0852 and NGC 1501, where $M_{\rm Astr} > M_{\rm Seis}$, as well as HS 2324+3944 and NGC 3271, which exhibit $M_{\rm Astr} < M_{\rm Seis}$.

Finally, in Fig. 25, we explore the compatibility between spectroscopic and astrometric masses. Once again, the large size of the error bars associated with the spectroscopic masses is noteworthy, indicating the substantial uncertainties in deriving $\log g$ through spectroscopy. In this case, the Pearson coefficient is $r = +0.06$, indicating again a negligible linear correlation. The average of the mass differences is in this case $\langle \Delta M_\star \rangle = 0.013\,M_\odot$, and the agreement limits are $\langle \Delta M_\star \rangle \pm 0.101\,M_\odot$. Also notable in this case is the strong discrepancy between the spectroscopic mass and the astrometric mass in several objects, such as NGC 1501, SDSS J0754+0852, NGC 246, and RX J2117+3412.

In summary, there is consensus among the sets of stellar masses for some GW Vir stars derived using three (or four) different methods, although there are outliers where mass determi-

nations by various methods display significant discrepancies. In the following, we delve into each of these cases.

- HS 2324+3944: For this star, we find $M_{\rm Seis}(\Delta\Pi) > M_{\rm Seis} > M_{\rm Astr} \simeq M_{\rm Spec}$. This suggests that the seismological masses are overestimated, particularly the one based on period spacing, while the spectroscopic mass, which closely matches the astrometric mass, appears to be well-determined.
- NGC 2371: The situation for this star is analogous to the case of HS 2324+3944, where the different estimates of the stellar mass verify the inequalities $M_{\rm Seis}(\Delta\Pi) > M_{\rm Seis} > M_{\rm Astr} \gtrsim M_{\rm Spec}$. So, again, we conclude that the seismological masses are overestimated.
- RX J2117+3412: This star presents a notable scenario where $M_{\rm Spec} > M_{\rm Astr} \gtrsim M_{\rm Seis}(\Delta\Pi) \gtrsim M_{\rm Astr}$. Unlike previous cases, the spectroscopic mass of RX J2117+3412 appears to be overstated, suggesting a potential need to re-assess the parameters $T_{\rm eff}$ and $\log g$ derived from spectroscopic analysis.
- NGC 246: This is a twin case to the RX J2117+3412 case ($M_{\rm Spec} > M_{\rm Astr} \gtrsim M_{\rm Seis}(\Delta\Pi) \gtrsim M_{\rm Astr}$). We suggest that the spectroscopic parameters of NGC 246, and thus the evaluation of its spectroscopic mass, need to be revised. Both NGC 246 and RX J2117+3412 exhibit P Cygni line profiles in the ultraviolet wavelength region that allowed their mass-loss rates to be measured (Koesterke & Werner 1998). It would be worthwhile to repeat the analysis of their optical spectra using expanding model atmospheres instead of hydrostatic ones that were employed to determine the spectroscopic parameters.
- NGC 1501: In this case, we find $M_{\rm Astr} > M_{\rm Seis} \simeq M_{\rm Seis}(\Delta\Pi) \gtrsim M_{\rm Spec}$. In this way, we conclude that the seismological and spectroscopic masses of NGC 1501 are quite low, and then $T_{\rm eff}$ and $\log g$ need to be revised. We remark

Fig. 24. Similar to Fig. 22, this figure displays the comparison between seismological and astrometric masses.
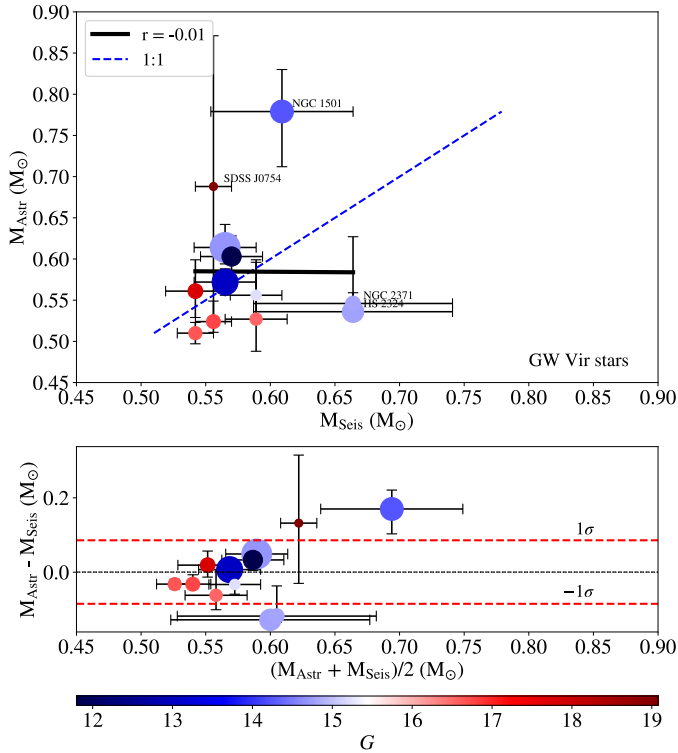

Fig. 25. In analogy to Fig. 22, this figure illustrates the comparison between spectroscopic and astrometric masses.

that it is not trivial to determine effective temperature and surface gravity of [WR] stars, because they have extended atmospheres. One has to define precisely the stellar radius, as this affects the values of temperature and gravity. In addition, using such atmosphere models as boundary conditions for evolution calculations could be significant for the location of the tracks in the Hertzsprung-Russell Diagram (HRD).

- SDSS J0754+0852: For this star, we have $M_{\rm Astr} > M_{\rm Seis} > M_{\rm Spec}$, the situation being completely analogous to the case of NGC 1501: the seismological and spectroscopic masses are quite small. We suggest revising the seismological and spectroscopic masses and reevaluating the spectroscopic parameters of SDSS J0754+0852. We note, however, that the astrometric mass error is the largest of all GW Vir stars because it is very faint.

5. Discussion

The results of the previous section point to several cases of important discrepancies between the masses derived through different methods for the three classes of pulsating WDs examined. In particular, we found situations in which the spectroscopic mass is in significant disagreement with the other mass determinations. In other cases, it is the seismological mass that is dissonant. In this section, we discuss some of the possible reasons that could explain, at least in part, the discrepancies found.

When considering stars with spectroscopic masses that disagree with other determinations, it becomes apparent that the uncertainties in determining $M_{\rm Spec}$ for WDs are closely related to uncertainties in determining the effective temperature and surface gravity. The accuracy of spectroscopic determinations depends heavily on the input physics incorporated into atmosphere models, particularly with respect to the reliability of modelled line profiles, especially in ultraviolet and optical spectra.
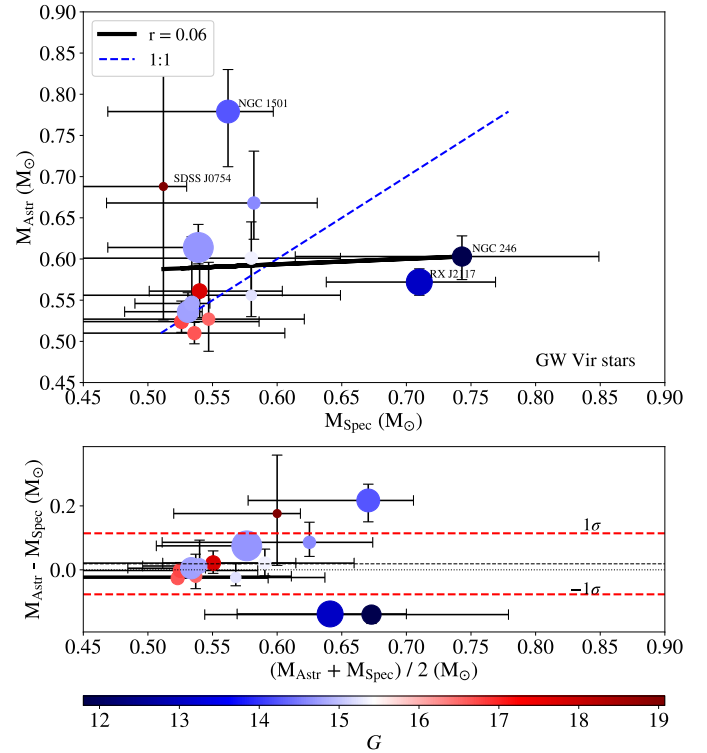
Factors such as line broadening and convective energy transport significantly influence the shape and intensity of spectral lines (Saumon et al. 2022).

Various systematic effects impact the assessment of $T_{\rm eff}$ and $\log g$ for WDs, particularly pulsating WDs. Fuchs (2017) spectroscopically observed 122 DA WDs that either pulsate or are close to the DAV instability strip and estimated $T_{\rm eff}$ and $\log g$ for each WD based on Balmer line profile shapes. They conducted a meticulous study of several systematics involved in data reduction and spectral fitting procedures, including extinction correction, flux calibration, and signal-to-noise ratios of the spectra, which can affect the final atmospheric parameters $T_{\rm eff}$ and $\log g$. They concluded that neglecting these systematic effects could introduce errors in atmospheric parameter determinations, potentially affecting the determination of spectroscopic masses for DAVs.

Similarly to DAVs, the determination of $T_{\rm eff}$ and $\log g$ for DBVs is subject to uncertainties arising from various sources, such as the input physics of atmosphere models, signal-to-noise ratio of spectra, use of different data sets, and accuracy of flux calibrations (see, e.g., Izquierdo et al. 2023). Specifically, in the case of the model atmosphere fit, precise values of $T_{\rm eff}$ are difficult to obtain within the range of ~21 000−31 000 K. Here, a plateau in the strength of the HeI absorption lines results in hot and cold solutions for $T_{\rm eff}$ due to the insensitivity of these lines to changes in temperature (Bergeron et al. 2011). This overlap with the DBV instability strip complicates their characterisation (Vanderbosch et al. 2022).

Notably, the photometric method provides an alternative value of the effective temperature as part of the fitting process itself, as previously mentioned. In fact, the photometric technique in DA WDs appears to be more accurate than the spectroscopic technique for the $T_{\rm eff}$ determination, as Genest-Beaulieu & Bergeron (2019a) show. However, these

authors also state that both techniques have a similar accuracy at determining the stellar masses of DA WDs. For DB WDs, Genest-Beaulieu & Bergeron (2019b) report that both techniques yield the effective temperature with comparable accuracy, but the photometric technique is a superior option for the estimation of WD masses. Overall, this technique is generally more advantageous because broadband fluxes are significantly less affected by the complexities of the atomic physics and the equation-of-state compared to line profiles. Nonetheless, its accuracy relies on the photometric calibration (Serenelli et al. 2021).

Finally, both T_{eff} and $\log g$ in GW Vir stars exhibit considerable uncertainties. As shown in Table A.3, T_{eff} uncertainties are generally manageable, typically within 10%. When UV spectra or high-resolution and high S/N ratio optical spectra are available, the error can decrease to approximately 5%. In particular, the presence of metal lines, often found in UV or optical spectra, serves as a valuable tool to constrain T_{eff} (Werner & Rauch 2014). However, $\log g$ uncertainties pose a significant challenge. Although errors for DAs and DBs typically hover around 0.05 dex, they can escalate to approximately 0.5 dex for GW Vir stars, with only a few exceptions as low as 0.3 or 0.2 dex, as detailed in Table A.3. The main problem is that the primary gravity indicator, the wings of the HeII line, exhibits weak sensitivity to variations of $\log g$, which directly affects the determination of gravity. Existent uncertainties in line-broadening theory also affect this determination. Moreover, the normalisation of optical spectra introduces systematic errors due to challenges in determining the true continuum, particularly given the width of the HeII (and CIV) lines. It is important to note that in the determinations of $\log g$ of GW Vir stars from the Tübingen group (see, e.g., Werner & Herwig 2006) not only are internal errors taken into account, coming from spectrum fits, but systematic errors are also accounted for, an aspect that may explain the relatively higher values of the uncertainty of $\log g$ compared to the other classes of pulsating WD stars studied in this work.

When considering stars with notably discrepant seismological masses, it becomes apparent that revisions may be necessary in the derivation of seismological models. Our analysis suggests that neither the number of pulsation periods nor the apparent brightness of pulsating WDs can be directly linked to the reliability of M_{Seis} determination. Specifically, having numerous periods available for asteroseismology does not guarantee the identification of a single and robust seismological solution. Instead, it is the distribution of these periods, particularly in terms of radial order, that significantly influences solution uniqueness or degeneracy. This issue has been exemplified in the case of DAVs by Giammichele et al. (2017), who demonstrated that even with a limited number of modes, precise determination of core chemical stratification can be achieved due to the considerable sensitivity of certain confined modes to partial mode trapping effects. Moreover, they highlighted that the ability to unravel the core structure and obtain a unique seismological model depends on the information content of available seismological data in terms of the weight functions[7] of the observed g-modes. In some cases, the isolation of a unique and well-defined seismological solution can prove challenging, leaving the problem degenerate. An additional factor contributing to potential errors in seismological model derivation is the inherent symmetry observed in high-overtone stellar pulsations as they probe

both the core and envelope of pulsating WDs (Montgomery et al. 2003). This symmetry has the potential to introduce ambiguity in the derived internal structure locations, as well as in the seismological models themselves. Finally, the choice of the asteroseismological approach and the criteria for selecting seismological models, when faced with a range of potential solutions, may influence the determination of the seismological mass, eventually leading to discrepancies compared to masses derived from other methods. In other cases, for stars with a limited number of periods, seismological analyses may resort to models constrained by external parameters such as spectroscopic T_{eff} and $\log g$. In these instances, we observe an obvious close alignment between the seismological and spectroscopic masses.

We close this section by pointing out that there could be possible systematic uncertainties in the WD evolutionary tracks that would affect the determination of the four types of mass determination, including the astrometric mass because this method uses the luminosity versus the effective temperature extracted from the evolutionary tracks, as well as the photometric mass, because of the use of the mass-radius relationships. It is important for future studies of this nature to employ alternative sets of WD evolutionary tracks, distinct from those used in this paper generated using the LPCODE evolutionary code. Concerning our results regarding the masses of the DAVs, the observed dispersion across various methods becomes particularly notable for masses exceeding approximately 0.75 $M_{\odot}$ (Figs. 8, 9, 10, and 11). Assessing whether this phenomenon reflects genuine discrepancies rooted in unexplored aspects of WD structure and evolution requires the examination of a substantially larger sample of objects. Investigating such a broader dataset will be the primary focus of future research.

6. Conclusions

In this paper, we conduct a comparative analysis to determine the level of agreement between various methodologies used in determining the stellar mass of isolated pulsating WDs. We compute the stellar mass for a sample of selected DAV, DBV, and GW Vir stars using four distinct approaches: spectroscopy, asteroseismology, astrometry, and photometry (although the latter was only applied for DAVs and DBVs). Specifically, we used the spectroscopic measurements of T_{eff} and $\log g$, along with WD evolutionary tracks, to estimate spectroscopic masses. Seismological mass values were sourced from the existing literature. Additionally, we derived astrometric masses using evolutionary tracks, spectroscopic effective temperatures, apparent magnitudes, and geometric distances obtained from *Gaia* parallaxes, as well as bolometric corrections from model atmospheres. We also utilised photometric masses and photometric effective temperatures from the literature, which have been determined using *Gaia* parallaxes and photometry combined with synthetic fluxes from model atmospheres. These values are then integrated with our evolutionary tracks to derive our own photometric masses. Our methodology involved employing identical evolutionary tracks and WD models in all methods. In particular, for assessing spectroscopic, astrometric, and photometric masses, we applied the same evolutionary tracks linked to sets of WD stellar models used in the asteroseismological analyses to derive seismological masses. This approach ensures coherence and reliability in comparing the four estimates of stellar mass.

The results of our analysis vary according to the category of pulsating WD considered. For DAVs, there is broad consensus among the four methods for stars with masses up to around ~0.75 $M_{\odot}$, but significant inconsistencies emerge for more

---

[7] Weight functions pinpoint the internal regions of the star that influence the period of the mode, providing insight into its sensitivity to specific parts (Kawaler et al. 1985; Townsend & Kawaler 2023).

massive DAVs (Figs. 8, 9, 10, and 11). Assessing whether this phenomenon reflects genuine discrepancies rooted in unexplored aspects of WD structure and evolution requires the examination of a substantially larger sample of objects. Investigating such a broader dataset will be the primary focus of future research. Regarding the examined DBVs, almost all objects in the sample exhibit astrometric masses that surpass their seismological, spectroscopic, and photometric counterparts (Figs. 16, 17, and 19). Finally, for GW Vir stars, while some display strong agreement among $M_{\rm Spec}$, $M_{\rm Seis}$, and $M_{\rm Astr}$, others reveal substantial disparities (Figs. 22, 23, 24 and 25). The dispersion of $M_\star$ values of the three classes of pulsating WDs considered in this paper, depending on the method used, suggests the need to re-assess the derivation of spectroscopic parameters ($T_{\rm eff}$ and $\log g$), as well as to revise the seismological models for some stars. Also, there is a need to continue improvements in the parallax measurements to exclude any possible astrometric error.

Future spectroscopic and photometric observations of pulsating WDs, particularly those deficient in H, are crucial for a more thorough comparison of these stars. We emphasise the importance of discovering pulsating WDs in eclipsing binaries, as this provides an opportunity to independently test seismological models. Ongoing and forthcoming large-scale spectroscopic surveys such as the Large Sky Area Multi-Object Fiber Spectroscopic Telescope (LAMOST; Cui et al. 2012), Sloan Digital Sky Survey V (SDSS-V; Kollmeier et al. 2017), WEAVE (Dalton et al. 2012), and 4MOST (de Jong et al. 2019) will play a significant role in confirming the spectroscopic classifications of pulsating WDs and expanding the sample size. Furthermore, ongoing and upcoming photometric observations from space missions such as the Transiting Exoplanet Survey Satellite (TESS; Ricker et al. 2015) and (PLATO; Rauer et al. 2014), respectively, as well as ground-based initiatives such as the Large Synoptic Survey Telescope (LSST; Ivezić et al. 2019) and BlackGEM (Bloemen et al. 2016), will offer valuable insights into the nature of variability among pulsating WDs and allow the discovery of more pulsation periods for better modelling.

References

Althaus, L. G., & Córsico, A. H. 2022, A&A, 663, A167
Althaus, L. G., Panei, J. A., Miller Bertolami, M. M., et al. 2009, ApJ, 704, 1605
Althaus, L. G., Córsico, A. H., Isern, J., & García-Berro, E. 2010, A&ARv, 18, 471
Altman, D. G., & Bland, J. M. 1983, Statistician, 32, 307
Bailer-Jones, C. A. L., Rybizki, J., Fouesneau, M., Demleitner, M., & Andrae, R. 2021, AJ, 161, 147
Bédard, A., Bergeron, P., Brassard, P., & Fontaine, G. 2020, ApJ, 901, 93
Bedin, L. R., Salaris, M., Piotto, G., et al. 2009, ApJ, 697, 965
Bedin, L. R., Salaris, M., Anderson, J., et al. 2015, MNRAS, 448, 1779
Bell, K. J., Córsico, A. H., Bischoff-Kim, A., et al. 2019, A&A, 632, A42
Benesty, J., Chen, J., Huang, Y., & Cohen, I. 2009, Noise Reduction in Speech Processing (New York: Springer), 37
Bergeron, P., Saffer, R. A., & Liebert, J. 1992, ApJ, 394, 228
Bergeron, P., Wesemael, F., & Beauchamp, A. 1995, PASP, 107, 1047
Bergeron, P., Ruiz, M. T., & Leggett, S. K. 1997, ApJS, 108, 339
Bergeron, P., Leggett, S. K., & Ruiz, M. T. 2001, ApJS, 133, 413
Bergeron, P., Wesemael, F., Dufour, P., et al. 2011, ApJ, 737, 28
Bergeron, P., Dufour, P., Fontaine, G., et al. 2019, ApJ, 876, 67
Bloemen, S., Groot, P., Woudt, P., et al. 2016, SPIE Conf. Ser., 9906
Bognár, Z., Paparó, M., Córsico, A. H., Kepler, S. O., & Győrffy, Á. 2014, A&A, 570, A116
Bond, H. E., Gilliland, R. L., Schaefer, G. H., et al. 2015, ApJ, 813, 106
Bond, H. E., Bergeron, P., & Bédard, A. 2017a, ApJ, 848, 16
Bond, H. E., Schaefer, G. H., Gilliland, R. L., et al. 2017b, ApJ, 840, 70
Caiazzo, I., Burdge, K. B., Fuller, J., et al. 2021, Nature, 595, 39
Calcaferro, L. M., Córsico, A. H., & Althaus, L. G. 2016, A&A, 589, A40
Calcaferro, L. M., Sowicka, P., Uzundag, M., et al. 2024, A&A, 686, A140
Camisassa, M. E., Althaus, L. G., Córsico, A. H., et al. 2019, A&A, 625, A87
Campos, F., Kepler, S. O., Bonatto, C., & Ducati, J. R. 2013, MNRAS, 433, 243
Campos, F., Bergeron, P., Romero, A. D., et al. 2016, MNRAS, 456, 3729
Catalán, S., Isern, J., García-Berro, E., & Ribas, I. 2008, MNRAS, 387, 1693
Chambers, K. C., Magnier, E. A., Metcalfe, N., et al. 2016, ArXiv e-prints [arXiv:1612.05560]
Ciardullo, R., & Bond, H. E. 1996, AJ, 111, 2332
Córsico, A. H. 2020, Front. Astron. Space Sci., 7, 47
Córsico, A. H. 2022, Boletin de la Asociacion Argentina de Astronomia La Plata Argentina, 63, 48
Córsico, A. H., & Althaus, L. G. 2006, A&A, 454, 863
Córsico, A. H., Miller Bertolami, M. M., Althaus, L. G., Vauclair, G., & Werner, K. 2007, A&A, 475, 619
Córsico, A. H., Althaus, L. G., Miller Bertolami, M. M., & García-Berro, E. 2009, A&A, 499, 257
Córsico, A. H., Althaus, L. G., Miller Bertolami, M. M., & Bischoff-Kim, A. 2012, A&A, 541, A42
Córsico, A. H., Althaus, L. G., Miller Bertolami, M. M., & Kepler, S. O. 2019a, A&ARv, 27, 7
Córsico, A. H., De Gerónimo, F. C., Camisassa, M. E., & Althaus, L. G. 2019b, A&A, 632, A119
Córsico, A. H., Uzundag, M., Kepler, S. O., et al. 2021, A&A, 645, A117
Córsico, A. H., Uzundag, M., Kepler, S. O., et al. 2022a, A&A, 668, A161
Córsico, A. H., Uzundag, M., Kepler, S. O., et al. 2022b, A&A, 659, A30
Cox, A. N. 2000, Allen's Astrophysical Quantities
Cui, X.-Q., Zhao, Y.-H., Chu, Y.-Q., et al. 2012, Res. Astron. Astrophys., 12, 1197
Cukanovaite, E., Tremblay, P. E., Freytag, B., Ludwig, H. G., & Bergeron, P. 2018, MNRAS, 481, 1522
Cummings, J. D., Kalirai, J. S., Choi, J., et al. 2019, ApJ, 871, L18
Dalton, G., Trager, S. C., Abrams, D. C., et al. 2012, SPIE Conf. Ser., 8446, 84460
de Jong, R. S., Agertz, O., Berbel, A. A., et al. 2019, Messenger, 175, 3
Doherty, C. L., Gil-Pons, P., Lau, H. H. B., et al. 2014, MNRAS, 441, 582
Dreizler, S., Werner, K., Heber, U., & Engels, D. 1996, A&A, 309, 820
Dufour, P., Blouin, S., Coutu, S., et al. 2017, ASP Conf. Ser., 509, 3
El-Badry, K., Rix, H.-W., & Weisz, D. R. 2018, ApJ, 860, L17
Fitzpatrick, E. L. 2004, ASP Conf. Ser., 309, 33
Fontaine, G., & Brassard, P. 2008, PASP, 120, 1043
Fontaine, G., Brassard, P., & Bergeron, P. 2001, PASP, 113, 409
Fuchs, J. T. 2017, PhD Thesis, University of North Carolina, Chapel Hill, USA
Gaia Collaboration 2020, VizieR Online Data Catalog, I/350
Gaia Collaboration (Vallenari, A., et al.) 2023, A&A, 674, A1
García-Berro, E., & Oswalt, T. D. 2016, New Astron. Rev., 72, 1
García-Berro, E., Torres, S., Althaus, L. G., et al. 2010, Nature, 465, 194
Genest-Beaulieu, C., & Bergeron, P. 2019a, ApJ, 871, 169
Genest-Beaulieu, C., & Bergeron, P. 2019b, ApJ, 882, 106
Gentile Fusillo, N. P., Tremblay, P.-E., Gänsicke, B. T., et al. 2019, MNRAS, 482, 4570
Gentile Fusillo, N. P., Tremblay, P. E., Cukanovaite, E., et al. 2021, MNRAS, 508, 3877
Giammichele, N., Charpinet, S., Brassard, P., & Fontaine, G. 2017, A&A, 598, A109
Giammichele, N., Charpinet, S., Fontaine, G., et al. 2018, Nature, 554, 73
Giavarina, D. 2015, Biochem. Med, 25, 141
Green, G. M., Schlafly, E. F., Finkbeiner, D., et al. 2018, MNRAS, 478, 651
Hansen, C. J., Kawaler, S. D., & Trimble, V. 2004, Stellar Interiors: Physical Principles, Structure, and Evolution (Berlin: Springer-Verlag)
Herald, J. E., & Bianchi, L. 2004, ApJ, 609, 378
Holberg, J. B., & Bergeron, P. 2006, AJ, 132, 1221
Hügelmeyer, S. D., Dreizler, S., Homeier, D., et al. 2006, A&A, 454, 617
Ivezić, Ž., Kahn, S. M., Tyson, J. A., et al. 2019, ApJ, 873, 111
Izquierdo, P., Gänsicke, B. T., Rodríguez-Gil, P., et al. 2023, MNRAS, 520, 2843
Kawaler, S. D. 1987, in IAU Colloq. 95: Second Conference on Faint Blue Stars, eds. A. G. D. Philip, D. S. Hayes, & J. W. Liebert, 297
Kawaler, S. D., Winget, D. E., & Hansen, C. J. 1985, ApJ, 295, 547
Kepler, S. O., Fraga, L., Winget, D. E., et al. 2014, MNRAS, 442, 2278
Kilic, M., Allende Prieto, C., Brown, W. R., & Koester, D. 2007, ApJ, 660, 1451

Kilic, M., Munn, J. A., Harris, H. C., et al. 2017, ApJ, 837, 162

Kippenhahn, R., Weigert, A., & Weiss, A. 2013, Stellar Structure and Evolution (Berlin: Springer)

Kleinman, S. J., Kepler, S. O., Koester, D., et al. 2013, ApJS, 204, 5

Koesterke, L., & Hamann, W. R. 1997, A&A, 320, 91

Koesterke, L., & Werner, K. 1998, ApJ, 500, L55

Kollmeier, J. A., Zasowski, G., Rix, H. W., et al. 2017, ArXiv e-prints [arXiv:1711.03234]

Liebert, J., Bergeron, P., & Holberg, J. B. 2005, ApJS, 156, 47

Löbling, L. 2020, IAU Symp., 357, 158

Miller Bertolami, M. M., & Althaus, L. G. 2006, A&A, 454, 845

Montgomery, M. H., Metcalfe, T. S., & Winget, D. E. 2003, MNRAS, 344, 657

Oliveira da Rosa, G., Kepler, S. O., Córsico, A. H., et al. 2022, ApJ, 936, 187

Parsons, S. G., Gänsicke, B. T., Marsh, T. R., et al. 2017, MNRAS, 470, 4473

Pasquini, L., Pala, A. F., Ludwig, H. G., et al. 2019, A&A, 627, L8

Rauer, H., Catala, C., Aerts, C., et al. 2014, Exp. Astron., 38, 249

Reed, M. D., Kawaler, S. D., & O'Brien, M. S. 2000, ApJ, 545, 429

Renedo, I., Althaus, L. G., Miller Bertolami, M. M., et al. 2010, ApJ, 717, 183

Ricker, G. R., Winn, J. N., Vanderspek, R., et al. 2015, J. Astron. Telesc. Instrum. Syst., 1, 014003

Rolland, B., Bergeron, P., & Fontaine, G. 2018, ApJ, 857, 56

Romero, A. D., Córsico, A. H., Althaus, L. G., et al. 2012, MNRAS, 420, 1462

Romero, A. D., Kepler, S. O., Córsico, A. H., Althaus, L. G., & Fraga, L. 2013, ApJ, 779, 58

Romero, A. D., Córsico, A. H., Castanheira, B. G., et al. 2017, ApJ, 851, 60

Romero, A. D., Amaral, L. A., Klippel, T., et al. 2019a, MNRAS, 490, 1803

Romero, A. D., Kepler, S. O., Joyce, S. R. G., Lauffer, G. R., & Córsico, A. H. 2019b, MNRAS, 484, 2711

Romero, A. D., Kepler, S. O., Hermes, J. J., et al. 2022, MNRAS, 511, 1574

Romero, A. D., da Rosa, G. O., Kepler, S. O., et al. 2023, MNRAS, 518, 1448

Saumon, D., Blouin, S., & Tremblay, P.-E. 2022, Phys. Rep., 988, 1

Schlegel, D. J., Finkbeiner, D. P., & Davis, M. 1998, ApJ, 500, 525

Serenelli, A., Weiss, A., Aerts, C., et al. 2021, A&ARv, 29, 4

Sowicka, P., Handler, G., Jones, D., et al. 2023, ApJS, 269, 32

Townsend, R. H. D., & Kawaler, S. D. 2023, Res. Notes Am. Astron. Soc., 7, 166

Tremblay, P. E., & Bergeron, P. 2009, ApJ, 696, 1755

Tremblay, P. E., Ludwig, H. G., Steffen, M., & Freytag, B. 2013, A&A, 559, A104

Tremblay, P. E., Cukanovaite, E., Gentile Fusillo, N. P., Cunningham, T., & Hollands, M. A. 2019, MNRAS, 482, 5222

Uzundag, M., Córsico, A. H., Kepler, S. O., et al. 2021, A&A, 655, A27

Uzundag, M., De Gerónimo, F. C., Córsico, A. H., et al. 2023, MNRAS, 526, 2846

Vanderbosch, Z. P., Hermes, J. J., Winget, D. E., et al. 2022, ApJ, 927, 158

Weidemann, V. 1977, A&A, 59, 411

Werner, K., & Herwig, F. 2006, PASP, 118, 183

Werner, K., & Rauch, T. 2014, A&A, 569, A99

Werner, K., Rauch, T., & Kruk, J. W. 2005, A&A, 433, 641

Werner, K., Rauch, T., Kruk, J. W., & Kurucz, R. L. 2011, A&A, 531, A146

Werner, K., Rauch, T., & Kepler, S. O. 2014, A&A, 564, A53

Winget, D. E., & Kepler, S. O. 2008, ARA&A, 46, 157

York, D. G., Adelman, J., Anderson, J. E., Jr, et al. 2000, AJ, 120, 1579

Appendix A: Lists of selected objects

In this appendix, we provide tables containing basic information about all the objects analysed in this paper. Table A.1 corresponds to DAV stars, Table A.2 is associated with DBV stars, and Table A.3 is for GW Vir stars.

Table A.1. Sample of the 37 DAV stars analysed in this study. In column (a), we show the star names, while columns (b) and (c) correspond to the equatorial coordinates. Column (d) corresponds to the V apparent magnitude, and columns (e), (f), and (g) display the DR3 *Gaia* apparent magnitudes. Column (h) depicts the spectral type, while columns (i) and (j) show the spectroscopic effective temperature and surface gravity, respectively, with 3D corrections (following Tremblay et al. 2013) applied. Finally, column (k) shows the DR3 *Gaia* parallax (Gaia Collaboration 2023), column (l) depicts the geometric distance from Bailer-Jones et al. (2021) based on the DR3 *Gaia* parallax. The last column (m) corresponds to the references from which $T_{\rm eff}$ and $\log g$ have been extracted.

Name	RA (deg)	DEC (deg)	V (mag)	G (mag)	$G_{\rm BP}$ (mag)	$G_{\rm RP}$ (mag)	S. Type	$T_{\rm eff}$ (K)	$\log g$ (cgs)	π (mas)	$d_{\rm BJ}$ (pc)	Reference
(a)	(b)	(c)	(d)	(e)	(f)	(g)	(h)	(i)	(j)	(k)	(l)	(m)
GD 244	344.193167	12.880681	15.788 ± 0.022	15.761	15.779	15.762	DA	11760 ± 200	8.09 ± 0.05	$15.98^{+0.04}_{-0.05}$	$62.46^{+0.16}_{-0.17}$	Córsico et al. (2019a)
G 226−29	252.107958	59.054969	12.306 ± 0.006	12.279	12.278	12.296	DA	12510 ± 200	8.35 ± 0.05	$91.34^{+0.05}_{-0.04}$	$10.95^{+0.07}_{-0.01}$	Córsico et al. (2019a)
HS 0507+0434B	77.556340	4.648649	15.403 ± 0.025	15.376	15.383	15.380	DA4.6	12010 ± 200	8.19 ± 0.05	$20.13^{+0.04}_{-0.04}$	$49.57^{+0.01}_{-0.01}$	Córsico et al. (2019a)
EC 11507−1519	178.313576	−15.610141	16.058 ± 0.013	16.031	16.046	16.042	DA4.4	12440 ± 200	8.20 ± 0.05	$14.03^{+0.06}_{-0.03}$	$71.05^{+0.33}_{-0.29}$	Córsico et al. (2019a)
L 19−2	218.281819	−81.337256	13.452 ± 0.008	13.424	13.429	13.451	DA	12070 ± 200	8.13 ± 0.05	$47.88^{+0.02}_{-0.02}$	$20.87^{+0.01}_{-0.01}$	Córsico et al. (2019a)
MCT 2148−2911	327.916151	−28.948080	16.074 ± 0.018	16.047	16.061	16.053	DA	12220 ± 52	7.97 ± 0.01	$13.51^{+0.05}_{-0.04}$	$73.83^{+0.30}_{-0.28}$	Gaia Collaboration (2020)
EC 14012−1446	210.988205	−15.019605	15.742 ± 0.055	15.716	15.728	15.705	DA	12020 ± 200	8.18 ± 0.05	$16.82^{+0.05}_{-0.06}$	$59.28^{+0.27}_{-0.18}$	Córsico et al. (2019a)
EC 23487−2424	357.842043	−24.138146	15.382 ± 0.039	15.355	15.391	15.348	DA	11560 ± 200	8.09 ± 0.05	$20.02^{+0.03}_{-0.03}$	$49.83^{+0.08}_{-0.08}$	Córsico et al. (2019a)
GD 165	216.162167	9.286603	14.371 ± 0.013	14.344	14.340	14.369	DA	12220 ± 200	8.11 ± 0.05	$29.99^{+0.03}_{-0.03}$	$33.30^{+0.03}_{-0.03}$	Córsico et al. (2019a)
Ross 808	240.347167	36.807100	14.435 ± 0.018	14.408	14.437	14.387	DA	11120 ± 200	7.98 ± 0.05	$30.47^{+0.03}_{-0.02}$	$32.79^{+0.02}_{-0.03}$	Córsico et al. (2019a)
HL Tau−76	64.735991	27.296754	15.057 ± 0.027	15.030	15.051	15.016	DA	11470 ± 200	7.92 ± 0.05	$29.99^{+0.03}_{-0.02}$	$33.30^{+0.03}_{-0.03}$	Córsico et al. (2019a)
GALEX J004855.2+152149	12.229877	15.363531	18.738 ± 0.047	18.711	18.692	18.696	DA	11280 ± 131	8.17 ± 0.07	$30.47^{+0.02}_{-0.02}$	$32.79^{+0.02}_{-0.02}$	Córsico et al. (2019a)
SDSS J084314.05+043131.6	130.808592	4.525483	17.863 ± 0.021	17.835	17.887	17.813	DA	11220 ± 71	8.09 ± 0.04	$6.59^{+0.11}_{-0.10}$	$151.42^{+2.60}_{-2.60}$	Córsico et al. (2019a)
GALEX J125710.5+012423	194.293767	1.406382	18.694 ± 0.052	18.665	18.705	18.779	DA	11490 ± 156	8.30 ± 0.08	$4.38^{+0.29}_{-0.26}$	$227.07^{+9.43}_{-2.73}$	Córsico et al. (2019a)
2QZ J132350.3+010304	200.959465	1.051161	18.576 ± 0.040	18.549	18.563	18.569	DA	11380 ± 157	8.45 ± 0.06	$5.53^{+0.25}_{-0.23}$	$127.36^{+3.4}_{-3.4}$	Córsico et al. (2019a)
GALEX J161218.1+083028	243.075313	8.507868	17.833 ± 0.024	17.806	17.841	17.843	DA	12250 ± 126	8.29 ± 0.04	$7.77^{+0.13}_{-0.14}$	$128.36^{+2.15}_{-2.17}$	Córsico et al. (2019a)
SDSS J164115.61+352140.6	250.315059	35.361287	19.119 ± 0.046	19.092	19.174	19.091	DA	12025 ± 185	8.34 ± 0.11	$3.67^{+0.15}_{-0.14}$	$272.62^{+8.61}_{-5.95}$	Córsico et al. (2019a)
GALEX J165020.5+301021	252.585514	30.172546	18.179 ± 0.026	18.151	18.204	18.099	DA	10830 ± 80	8.43 ± 0.05	$7.74^{+0.11}_{-0.11}$	$128.32^{+1.89}_{-1.89}$	Córsico et al. (2019a)
GALEX J220830.0+065448	332.125111	6.913508	17.999 ± 0.035	17.972	18.003	17.974	DA	11147 ± 81	8.25 ± 0.04	$7.67^{+0.13}_{-0.11}$	$130.03^{+2.62}_{-1.13}$	Córsico et al. (2019a)
KIC 11911480	290.103625	50.289583	18.091 ± 0.030	18.064	18.122	18.079	DA	12160 ± 140	7.94 ± 0.04	$5.50^{+0.09}_{-0.08}$	$177.57^{+1.26}_{-0.99}$	Córsico et al. (2019a)
GD 1212	354.711542	−7.688981	13.320 ± 0.011	13.293	13.326	13.257	DA	10970 ± 140	8.03 ± 0.05	$53.58^{+0.02}_{-0.02}$	$18.65^{+0.01}_{-0.01}$	Córsico et al. (2019a)
GALEX J134550.9−005536	206.462178	−0.926792	16.787 ± 0.018	16.760	16.784	16.782	DA	11760 ± 40	8.10 ± 0.02	$9.93^{+0.09}_{-0.08}$	$100.82^{+0.54}_{-0.76}$	Córsico et al. (2019a)
SDSS J215905.5+132256	329.773050	13.382184	18.986 ± 0.065	18.959	19.027	18.978	DA	11370 ± 151	8.69 ± 0.06	$5.10^{+0.24}_{-0.25}$	$197.84^{+8.13}_{-9.25}$	Córsico et al. (2019a)
BPM 37093	189.707421	−49.800058	13.820 ± 0.007	13.793	13.819	13.771	DA	11620 ± 500	8.69 ± 0.05	$67.41^{+0.02}_{-0.02}$	$14.83^{+0.01}_{-0.01}$	Córsico et al. (2019a)
GD 518	254.812917	66.176461	17.271 ± 0.013	17.244	17.270	17.245	DA	11760 ± 210	8.97 ± 0.06	$15.48^{+0.06}_{-0.05}$	$64.52^{+0.23}_{-0.22}$	Córsico et al. (2019a)
TIC 8445665	246.153382	32.214668	16.732 ± 0.032	16.705	16.744	16.698	DA	11385 ± 235	7.95 ± 0.04	$10.24^{+0.06}_{-0.06}$	$97.35^{+0.56}_{-0.54}$	Romero et al. (2022)
TIC 46847635	142.319587	−8.675615	16.775 ± 0.014	16.748	16.768	16.785	DA	12018 ± 344	7.98 ± 0.05	$9.65^{+0.08}_{-0.08}$	$103.29^{+0.81}_{-0.78}$	Romero et al. (2022)
TIC 167486543	72.133797	−10.897180	16.260 ± 0.029	16.233	16.245	16.241	DA	12187 ± 252	8.55 ± 0.03	$18.20^{+0.05}_{-0.05}$	$54.82^{+0.17}_{-0.19}$	Romero et al. (2022)
TIC 441500792	46.701453	−17.392481	16.709 ± 0.046	16.683	16.713	16.671	DA	11393 ± 273	8.05 ± 0.05	$10.97^{+0.09}_{-0.08}$	$90.97^{+0.57}_{-0.51}$	Romero et al. (2022)
TIC 442962289	81.448483	−17.563872	16.535 ± 0.032	16.508	16.531	16.512	DA	11945 ± 252	8.42 ± 0.03	$14.74^{+0.06}_{-0.06}$	$67.69^{+0.25}_{-0.25}$	Romero et al. (2022)
TIC 686044219	65.454141	−35.980307	17.158 ± 0.045	17.131	17.148	17.118	DA	11477 ± 356	8.02 ± 0.06	$8.71^{+0.06}_{-0.06}$	$114.51^{+0.85}_{-0.57}$	Romero et al. (2022)
TIC 712406809	99.821860	1.224859	16.246 ± 0.036	16.218	16.201	16.130	DA	10669 ± 298	7.91 ± 0.07	$13.53^{+0.09}_{-0.09}$	$73.73^{+0.53}_{-0.53}$	Romero et al. (2022)
TIC 20979953	233.387357	−2.115480	16.540 ± 0.016	16.513	16.541	16.522	DA	11859 ± 236	7.97 ± 0.04	$10.93^{+0.11}_{-0.11}$	$91.24^{+0.70}_{-0.76}$	Romero et al. (2022)
TIC 55650407	73.863635	−62.979060	14.998 ± 0.015	14.971	14.984	14.984	DA	11838 ± 150	7.95 ± 0.02	$21.65^{+0.03}_{-0.02}$	$46.11^{+0.05}_{-0.05}$	Romero et al. (2022)
TIC 282783760	198.611837	17.535972	16.306 ± 0.023	16.279	16.278	16.285	DA	12111 ± 268	8.03 ± 0.03	$12.39^{+0.05}_{-0.05}$	$80.58^{+0.32}_{-0.30}$	Romero et al. (2022)
BPM 31594	55.870974	−45.817843	15.069 ± 0.035	15.042	15.063	15.039	DA	11500 ± 22	8.05 ± 0.01	$22.59^{+0.04}_{-0.04}$	$44.20^{+0.05}_{-0.05}$	Córsico et al. (2019a)
G 29−38	352.198485	5.248399	13.089 ± 0.029	13.062	13.084	13.053	DAZ	11910 ± 162	8.17 ± 0.04	$57.10^{+0.03}_{-0.03}$	$17.51^{+0.01}_{-0.01}$	Córsico et al. (2019a)

Table A.2. Sample of the nine DBV stars considered in this work. Each column contains information similar to that presented in Table A.1. In this case, column (m) gives the interstellar extinction measured in the V band, computed from the reddening $E(B - V)$ for each star. The spectroscopic effective temperature and surface gravity are those tabulated by Córsico et al. (2019a) that have been corrected by 3D effects following Cukanovaite et al. (2018), unless another reference is indicated.

Name	RA (deg)	DEC (deg)	V (mag)	G (mag)	G_{BP} (mag)	G_{RP} (mag)	S. Type	T_{eff} (K)	$\log g$ (cgs)	π (mas)	d_{BJ} (pc)	A_V (mag)	Reference
(a)	(b)	(c)	(d)	(e)	(f)	(g)	(h)	(i)	(j)	(k)	(l)	(m)	(n)
KIC 8626021	292.269496	44.785841	18.545 ± 0.033	18.500	18.409	18.692	DB	$28\,480 \pm 750$	7.89 ± 0.07	$2.65^{+0.11}_{-0.14}$	$382.39^{+13.54}_{-16.90}$	$0.152^{+0.017}_{-0.027}$	Córsico et al. (2019a)
KUV 05134+2605	79.115780	26.143762	16.795 ± 0.019	16.749	16.657	16.923	DBA	$24\,680 \pm 1300$	8.21 ± 0.06	$6.69^{+0.07}_{-0.07}$	$149.77^{+1.72}_{-1.80}$	$0.063^{+0.026}_{-0.027}$	Córsico et al. (2019a)
TIC 257459955	30.236306	-15.769369	14.707 ± 0.016	14.657	14.554	14.846	DB	$25\,500 \pm 1369$	7.88 ± 0.03	$14.57^{+0.04}_{-0.04}$	$68.51^{+0.12}_{-0.11}$	$0.025^{+0.027}_{-0.017}$	Córsico et al. (2019a)
GD 358	251.826636	32.475796	13.630 ± 0.020	13.580	13.476	13.770	DB2.3	$24\,940 \pm 1018$	7.75 ± 0.05	$23.24^{+0.02}_{-0.03}$	$42.99^{+0.04}_{-0.05}$	$0.010^{+0.008}_{-0.007}$	Córsico et al. (2019a)
PG 1351+489	208.292000	48.672500	16.728 ± 0.024	16.678	16.586	16.877	DB	$26\,010 \pm 1536$	7.91 ± 0.07	$5.69^{+0.05}_{-0.05}$	$175.73^{+1.53}_{-1.53}$	$0.062^{+0.011}_{-0.019}$	Córsico et al. (2019a)
EC 20058−5234	302.416147	-52.421304	15.806 ± 0.016	15.756	15.647	15.938	DB	$25\,500 \pm 500$	8.01 ± 0.05	$8.48^{+0.05}_{-0.06}$	$117.95^{+0.68}_{-0.75}$	$0.181^{+0.108}_{-0.108}$	Córsico et al. (2019a)
EC 04207−4748	65.547319	-47.695004	15.280 ± 0.022	15.229	15.128	15.423	DB	$25\,970 \pm 545$	7.79 ± 0.06	$10.93^{+0.03}_{-0.03}$	$91.48^{+0.22}_{-0.23}$	$0.040^{+0.024}_{-0.024}$	Córsico et al. (2019a)
WD J152738.37−450207.3	231.909792	-45.035391	15.527 ± 0.018	15.482	15.375	15.634	DB	$25\,228 \pm 630$	8.12 ± 0.01	$10.54^{+0.04}_{-0.05}$	$94.62^{+0.34}_{-0.37}$	$0.927^{+0.566}_{-0.566}$	Córsico et al. (2022a)
L 7−44	263.228940	-87.167376	14.785 ± 0.011	14.737	14.639	14.918	DB	$23\,980 \pm 1686$	8.05 ± 0.03	$14.47^{+0.02}_{-0.01}$	$69.09^{+0.14}_{-0.12}$	$0.544^{+0.326}_{-0.326}$	Rolland et al. (2018)

Table A.3. Sample of the fourteen GW Vir stars considered in this work. Each column contains information similar to that presented in Table A.2. The spectroscopic effective temperature and surface gravity are those tabulated by Córsico et al. (2019a), unless another reference is indicated. Since PG 2131+066 lacks parallax data from *Gaia*, we are unable to obtain the Bailer-Jones et al. (2021)'s distance, therefore, we include here the distance derived by Reed et al. (2000) using the spectroscopic parallax of the M star, the primary component of the binary system to which PG 2131+066 belongs.

Name	RA (deg)	DEC (deg)	V (mag)	G (mag)	G_{BP} (mag)	G_{RP} (mag)	S. Type	T_{eff} (K)	log g (cgs)	π (mas)	d_{BJ} (pc)	A_V (mag)	Reference
(a)	(b)	(c)	(d)	(e)	(f)	(g)	(h)	(i)	(j)	(k)	(l)	(m)	(n)
PG 0122+200	21.343833	20.299097	16.845 ± 0.019	16.751	16.593	17.109	PG 1159	$80\,000 \pm 4000$	7.50 ± 0.50	$1.64^{+0.08}_{-0.07}$	618^{+42}_{-37}	$0.133^{+0.017}_{-0.008}$	Werner & Rauch (2014)
PG 2131+066	323.534167	6.849331	16.577 ± 0.100	16.545	16.356	16.160	PG 1159	$95\,000 \pm 5000$	7.50 ± 0.50	$\ldots$	681^{+170}_{-137}	$0.120^{+0.008}_{-0.022}$	Werner & Rauch (2014)
PG 1707+427	257.198625	42.683578	16.757 ± 0.027	16.648	16.452	17.027	PG 1159	$85\,000 \pm 5000$	7.50 ± 0.50	$1.40^{+0.05}_{-0.33}$	733^{+32}_{-26}	$0.145^{+0.006}_{-0.070}$	Werner & Rauch (2014)
SDSS J075415.12+085232.2	118.562991	8.875609	19.186 ± 0.046	18.078	18.925	19.495	PG 1159	$120\,000 \pm 10\,000$	7.00 ± 0.30	$0.57^{+0.23}_{-0.33}$	1800^{+1200}_{-500}	$0.095^{+0.014}_{-0.070}$	Werner et al. (2014)
SDSS J034917.41−005919.3	57.322537	−0.988675	17.845 ± 0.026	17.798	17.694	17.968	PG 1159	$90\,000 \pm 900$	7.50 ± 0.01	$1.15^{+0.18}_{-0.16}$	850^{+500}_{-200}	$0.392^{+0.020}_{-0.012}$	Hügelmeyer et al. (2006)
RX J2117.1+3412	319.284507	34.207616	13.120 ± 0.009	13.022	12.842	13.375	PG 1159	$170\,000 \pm 10\,000$	6.00 ± 0.03	$1.99^{+0.04}_{-0.04}$	499^{+8}_{-9}	$0.164^{+0.018}_{-0.027}$	Werner et al. (2005)
HS 2324+3944	351.816397	40.023175	14.821 ± 0.012	14.770	14.653	14.958	PG41159	$130\,000 \pm 10\,000$	6.20 ± 0.20	$0.70^{+0.05}_{-0.03}$	1400^{+74}_{-54}	$0.474^{+0.022}_{-0.013}$	Dreizler et al. (1996)
NGC 6905	305.595800	20.104524	14.634 ± 0.026	14.597	14.443	14.637	[WC3]	$141\,000 \pm 10\,000$	6.00 ± 0.20	$0.37^{+0.03}_{-0.03}$	2700^{+200}_{-200}	$0.266^{+0.063}_{-0.013}$	Ciardullo & Bond (1996)
NGC 2371	111.394535	29.490675	14.853 ± 0.025	14.778	14.620	15.053	[WO1]	$135\,000 \pm 10\,000$	6.30 ± 0.20	$0.58^{+0.03}_{-0.04}$	1692^{+143}_{-122}	$0.158^{+0.005}_{-0.018}$	Herald & Bianchi (2004)
NGC 1501	61.747467	60.920631	14.329 ± 0.023	14.237	14.470	13.873	[WO4]	$134\,000 \pm 10\,000$	6.00 ± 0.20	$0.58^{+0.02}_{-0.02}$	1645^{+54}_{-47}	$1.829^{+0.011}_{-0.011}$	Koesterke & Hamann (1997)
TIC 333432673	100.315183	−13.689936	15.290 ± 0.021	15.215	15.058	15.492	PG 1159	$120\,000 \pm 10\,000$	7.50 ± 0.50	$2.55^{+0.04}_{-0.04}$	389^{+7}_{-5}	$0.458^{+0.011}_{-0.142}$	Uzundag et al. (2021)
TIC 095332541	90.687447	−13.850989	15.413 ± 0.020	15.319	15.139	15.656	PG 1159	$120\,000 \pm 10\,000$	7.50 ± 0.50	$2.59^{+0.04}_{-0.03}$	384^{+5}_{-5}	$0.186^{+0.019}_{-0.026}$	Uzundag et al. (2021)
PG 1159−035	180.441555	−3.7612860	15.808 ± 0.015	14.693	14.485	14.080	PG 1159	$140\,000 \pm 5000$	7.00 ± 0.50	$1.69^{+0.06}_{-0.06}$	585^{+20}_{-21}	$0.063^{+0.076}_{-0.095}$	Werner et al. (2011)
NGC 246	11.763925	−11.871936	11.905 ± 0.012	11.797	11.597	12.169	PG 1159	$150\,000 \pm 10\,000$	5.70 ± 0.10	$1.88^{+0.02}_{-0.02}$	538^{+20}_{-20}	$0.148^{+0.120}_{-0.051}$	Löbling (2020)

Appendix B: Stellar mass tabulations

Table B.1. Stellar masses of the DAV star sample.

Star	$M_{\rm Spec}$ $[M_\odot]$	$M_{\rm Seis}$ $[M_\odot]$	N_Π	$M_{\rm Astr}$ $[M_\odot]$	$M_{\rm Phot}$ $[M_\odot]$
GD 244	0.656 ± 0.030	$0.593 \pm 0.012^{(1)}$	5	$0.651^{+0.025}_{-0.026}$	$0.614^{+0.027}_{-0.025}$
G 226−29	0.815 ± 0.032	$0.770 \pm 0.034^{(1)}$	1	$0.815^{+0.015}_{-0.012}$	$0.770^{+0.015}_{-0.014}$
HS 0507+0434B	0.715 ± 0.031	$0.660 \pm 0.023^{(1)}$	4	$0.715^{+0.021}_{-0.027}$	$0.675^{+0.028}_{-0.033}$
EC 11507−1519	0.722 ± 0.031	$0.705 \pm 0.033^{(1)}$	2	$0.691^{+0.018}_{-0.020}$	$0.620^{+0.025}_{-0.024}$
L 19−2	0.680 ± 0.030	$0.705 \pm 0.033^{(1)}$	5	$0.691^{+0.013}_{-0.017}$	$0.668^{+0.015}_{-0.015}$
MCT 2148−2911	0.591 ± 0.005	$0.632 \pm 0.014^{(1)}$	1	$0.650^{+0.023}_{-0.021}$	$0.589^{+0.027}_{-0.025}$
EC 14012−1446	0.709 ± 0.031	$0.632 \pm 0.014^{(1)}$	9	$0.697^{+0.036}_{-0.039}$	$0.632^{+0.054}_{-0.048}$
EC 23487−2424	0.655 ± 0.030	$0.770 \pm 0.034^{(1)}$	3	$0.667^{+0.031}_{-0.033}$	$0.620^{+0.034}_{-0.031}$
GD 165	0.668 ± 0.030	$0.632 \pm 0.014^{(1)}$	4	$0.660^{+0.018}_{-0.016}$	$0.639^{+0.018}_{-0.017}$
Ross 808	0.593 ± 0.028	$0.705 \pm 0.033^{(1)}$	17	$0.615^{+0.024}_{-0.025}$	$0.591^{+0.020}_{-0.019}$
HL Tau−76	0.563 ± 0.026	$0.548 \pm 0.012^{(1)}$	12	$0.571^{+0.025}_{-0.026}$	$0.532^{+0.027}_{-0.029}$
GALEX J0048+1521	0.702 ± 0.043	$0.949 \pm 0.014^{(2)}$	6	$0.821^{+0.067}_{-0.081}$	$0.852^{+0.066}_{-0.060}$
SDSS J0843+0431	0.655 ± 0.024	$0.837 \pm 0.021^{(2)}$	6	$0.662^{+0.028}_{-0.028}$	$0.594^{+0.026}_{-0.025}$
GALEX J1257+0124	0.782 ± 0.051	$0.705 \pm 0.023^{(2)}$	8	$0.668^{+0.059}_{-0.064}$	$0.744^{+0.053}_{-0.044}$
2QZ J1323+0103	0.876 ± 0.038	$0.917 \pm 0.020^{(2)}$	15	$1.049^{+0.037}_{-0.033}$	$0.820^{+0.040}_{-0.036}$
GALEX J1612+0830	0.776 ± 0.025	$0.705 \pm 0.023^{(2)}$	1	$0.874^{+0.023}_{-0.037}$	$0.830^{+0.024}_{-0.023}$
SDSS J1641+3521	0.808 ± 0.069	$0.721 \pm 0.025^{(2)}$	2	$0.721^{+0.046}_{-0.059}$	$0.596^{+0.049}_{-0.035}$
GALEX J1650+3010	0.863 ± 0.032	$1.024 \pm 0.013^{(2)}$	3	$0.877^{+0.028}_{-0.028}$	$0.824^{+0.027}_{-0.026}$
GALEX J2208+0654	0.750 ± 0.025	$0.949 \pm 0.014^{(2)}$	2	$0.832^{+0.028}_{-0.037}$	$0.825^{+0.033}_{-0.031}$
KIC 11911480	0.575 ± 0.021	$0.548 \pm 0.010^{(3)}$	5	$0.692^{+0.025}_{-0.026}$	$0.597^{+0.029}_{-0.023}$
GD 1212	0.620 ± 0.029	$0.632 \pm 0.014^{(3)}$	7	$0.641^{+0.018}_{-0.018}$	$0.609^{+0.017}_{-0.016}$
GALEX J1345−0055	0.662 ± 0.012	$0.686 \pm 0.011^{(4)}$	2	$0.636^{+0.017}_{-0.015}$	$0.611^{+0.016}_{-0.015}$
SDSS J2159+1322	1.012 ± 0.034	$0.917 \pm 0.040^{(4)}$	3	$0.881^{+0.069}_{-0.070}$	$0.928^{+0.060}_{-0.059}$
BPM 37093	1.012 ± 0.029	$1.160 \pm 0.014^{(5)}$	8	$1.045^{+0.029}_{-0.038}$	$1.010^{+0.010}_{-0.010}$
GD 518	1.158 ± 0.028	$1.220 \pm 0.030^{(5)}$	3	$1.117^{+0.017}_{-0.013}$	$1.106^{+0.020}_{-0.020}$
TIC 8445665	0.578 ± 0.021	$0.675^{(6)}$	5	$0.614^{+0.035}_{-0.034}$	$0.580^{+0.038}_{-0.034}$
TIC 46847635	0.595 ± 0.028	$0.686^{(6)}$	1	$0.628^{+0.032}_{-0.032}$	$0.597^{+0.047}_{-0.041}$
TIC 167486543	0.934 ± 0.017	$0.820^{(6)}$	2	$0.959^{+0.026}_{-0.025}$	$0.930^{+0.023}_{-0.023}$
TIC 441500792	0.632 ± 0.029	$0.705^{(6)}$	3	$0.660^{+0.044}_{-0.046}$	$0.630^{+0.048}_{-0.042}$
TIC 442962289	0.858 ± 0.019	$0.837^{(6)}$	3	$0.884^{+0.028}_{-0.036}$	$0.851^{+0.030}_{-0.030}$
TIC 686044219	0.616 ± 0.035	$0.639^{(6)}$	3	$0.649^{+0.047}_{-0.052}$	$0.616^{+0.059}_{-0.050}$
TIC 712406809	0.556 ± 0.037	$0.646^{(6)}$	5	$0.589^{+0.049}_{-0.048}$	$0.563^{+0.066}_{-0.062}$
TIC 20979953	0.590 ± 0.022	$0.593^{(6)}$	3	$0.631^{+0.031}_{-0.029}$	$0.591^{+0.038}_{-0.034}$
TIC 55650407	0.580 ± 0.011	$0.570^{(6)}$	4	$0.610^{+0.015}_{-0.018}$	$0.580^{+0.017}_{-0.016}$
TIC 282783760	0.623 ± 0.017	$0.593^{(6)}$	3	$0.662^{+0.028}_{-0.030}$	$0.621^{+0.031}_{-0.029}$
BPM 31594	0.632 ± 0.006	$0.632^{(7)}$	6	$0.643^{+0.015}_{-0.016}$	$0.622^{+0.032}_{-0.029}$
G 29−38	0.703 ± 0.025	$0.632 \pm 0.030^{(8)}$	38	$0.684^{+0.026}_{-0.022}$	$0.629^{+0.027}_{-0.025}$

Notes. The first column displays the star names, the second column corresponds to the spectroscopic stellar mass ($M_{\rm Spec}$), the third column shows the seismological mass ($M_{\rm Seis}$), the fourth column shows the number of g-mode periods employed to derive the seismological mode (N_Π), the fifth column corresponds to the astrometric mass ($M_{\rm Astr}$), and the sixth column corresponds to the photometric mass ($M_{\rm Phot}$). It is important to note that the sample is comprised solely of DAV stars with asteroseismological models characterised by a canonical H-envelope thickness. In the case of the stars analysed by Romero et al. (2022) and Romero et al. (2023), the uncertainties in the seismological masses are not available, as they have not been explicitly provided by the authors.
References. (1) Romero et al. (2012); (2) Romero et al. (2013); (3) Romero et al. (2017); (4) Romero et al. (2019a); (5) Córsico et al. (2019b); (6) Romero et al. (2022); (7) Romero et al. (2023); (8) Uzundag et al. (2023).

Table B.2. Stellar masses of the DBV star sample.

Star	$M_{\rm Spec}$ [$M_\odot$]	$M_{\rm Seis}$ [$M_\odot$]	$M_{\rm Seis(ps)}$ [$M_\odot$]	N_Π	$M_{\rm Astr}$ [$M_\odot$]	$M_{\rm Phot}$ [$M_\odot$]
KIC 8626021	0.553 ± 0.037	0.664 ± 0.077[1]	0.696 ± 0.031[1]	5	$0.747^{+0.059}_{-0.057}$	$0.680^{+0.049}_{-0.039}$
KUV 05134+2605	0.726 ± 0.039	0.840 ± 0.010[2]	0.850 ± 0.050[2]	16	$0.798^{+0.033}_{-0.034}$	$0.731^{+0.035}_{-0.033}$
TIC 257459955	0.542 ± 0.019	0.609 ± 0.055[3]	0.621 ± 0.057[3]	10	$0.651^{+0.024}_{-0.027}$	$0.596^{+0.022}_{-0.020}$
GD 358	0.561 ± 0.028	0.584 ± 0.025[4]	0.588 ± 0.024[4]	19	$0.616^{+0.025}_{-0.026}$	$0.579^{+0.034}_{-0.031}$
PG 1351+489	0.559 ± 0.040	0.664 ± 0.013[5]	0.740 to 0.870[5]	4	$0.648^{+0.047}_{-0.047}$	$0.598^{+0.038}_{-0.035}$
EC 20058−5234	0.611 ± 0.029	0.664 ± 0.013[5]	0.530 to 0.550[5]	11	$0.618^{+0.020}_{-0.020}$	$0.556^{+0.021}_{-0.018}$
EC 04207−4748	0.516 ± 0.026	0.542 ± 0.017[5]	0.565 ± 0.020[5]	4	$0.660^{+0.020}_{-0.019}$	$0.580^{+0.020}_{-0.018}$
WD J1527−4502	0.673 ± 0.007	0.542 ± 0.023[5]	$\cdots$	4	$0.694^{+0.018}_{-0.021}$	$0.574^{+0.028}_{-0.026}$
L 7−44	0.631 ± 0.020	0.565 ± 0.023[5]	$\cdots$	6	$0.651^{+0.031}_{-0.030}$	$0.594^{+0.026}_{-0.024}$

Notes. The first column displays the star names, the second column corresponds to the spectroscopic stellar mass ($M_{\rm Spec}$), the third column shows the seismological mass ($M_{\rm Seis}$), the fourth column corresponds to the seismological mass inferred from the measured period spacing ($M_{\rm Seis(ps)}$), the fifth column corresponds to the number of g-mode periods employed to derive the seismological model and the period spacing (N_Π), and the sixth and seventh columns are the astrometric ($M_{\rm Astr}$) and photometric ($M_{\rm Phot}$) masses, respectively.
References. (1) Córsico et al. (2012); (2) Bognár et al. (2014); (3) Bell et al. (2019); (4) Córsico et al. (2022b); (5) Córsico et al. (2022a).

Table B.3. Stellar masses of the GW Vir sample.

Star	$M_{\rm Spec}$ [$M_\odot$]	$M_{\rm Seis}$ [$M_\odot$]	$M_{\rm Seis(ps)}$ [$M_\odot$]	N_Π	$M_{\rm Astr}$ [$M_\odot$]
PG 0122+200	$0.526^{+0.172}_{-0.060}$	0.556 ± 0.014[1]	0.567 ± 0.013[1]	9	$0.524^{+0.028}_{-0.014}$
PG 2131+066	$0.547^{+0.174}_{-0.074}$	0.589 ± 0.024[2]	0.578 ± 0.022[2]	7	$0.527^{+0.082}_{-0.047}$
PG 1707+427	$0.536^{+0.172}_{-0.070}$	0.542 ± 0.014[2]	0.566 ± 0.024[2]	8	$0.510^{+0.025}_{-0.035}$
SDSS J0754+0852	$0.512^{+0.080}_{-0.018}$	0.556 ± 0.014[3]	$\cdots$	3	$0.688^{+0.184}_{-0.168}$
SDSS J0349−0059	$0.540^{+0.039}_{-0.064}$	0.542 ± 0.023[4]	0.535 ± 0.004[4]	10	$0.561^{+0.047}_{-0.033}$
RX J2117+3412	$0.710^{+0.072}_{-0.059}$	0.565 ± 0.024[5]	0.569 ± 0.015[5]	31	$0.572^{+0.018}_{-0.018}$
HS 2324+3944	$0.531^{+0.049}_{-0.011}$	0.664 ± 0.077[5]	0.727 ± 0.017[5]	21	$0.536^{+0.028}_{-0.015}$
NGC 6905	$0.582^{+0.114}_{-0.049}$	$\cdots$	0.506 to 0.818[5]	5	$0.668^{+0.067}_{-0.048}$
NGC 2371	$0.534^{+0.044}_{-0.014}$	0.664 ± 0.077[5]	0.760 ± 0.005[5]	10	$0.546^{+0.083}_{-0.018}$
NGC 1501	$0.562^{+0.093}_{-0.035}$	0.609 ± 0.055[5]	0.586 to 0.636[5]	24	$0.779^{+0.056}_{-0.071}$
TIC 333432673	$0.580^{+0.174}_{-0.069}$	0.589 ± 0.020[6]	0.600 ± 0.011[6]	5	$0.556^{+0.045}_{-0.027}$
TIC 095332541	$0.580^{+0.174}_{-0.069}$	$\cdots$	0.550 to 0.570[6]	7	$0.601^{+0.047}_{-0.042}$
PG 1159−035	$0.539^{+0.070}_{-0.010}$	0.565 ± 0.024[7]	0.536 to 0.581[7]	41	$0.614^{+0.031}_{-0.023}$
NGC 246	$0.743^{+0.129}_{-0.106}$	0.570 ± 0.024[8]	0.568 ± 0.012[8]	17	$0.603^{+0.026}_{-0.029}$

Notes. The first column displays the star names, the second column corresponds to the spectroscopic stellar mass ($M_{\rm Spec}$), the third column shows the seismological mass ($M_{\rm Seis}$), the fourth column corresponds to the seismological mass inferred from the measured period spacing ($M_{\rm Seis(ps)}$), the fifth column corresponds to the number of g-mode periods employed to derive the seismological model and the period spacing (N_Π), and the sixth column is the astrometric mass ($M_{\rm Astr}$).
References. (1) Córsico et al. (2007); (2) Córsico et al. (2009); (3) Kepler et al. (2014); (4) Calcaferro et al. (2016); (5) Córsico et al. (2021); (6) Uzundag et al. (2021); (7) Oliveira Rosa et al. (2022); (8) Calcaferro et al. (2024).

Table B.4. List of the outlier DAV stars.

Comparison	Outlier	$\Delta M_\star$ [$M_\odot$]	N_Π	G [mag]
$M_{\rm Spec}$ vs $M_{\rm Seis}$ ($\Delta M_\star \equiv M_{\rm Seis} - M_{\rm Spec}$)	BPM 37093	0.148	8	13.793
	GALEX J1650+3010	0.161	3	18.151
	GALEX J2208+0654	0.199	2	17.972
	GALEX J0048+1521	0.247	6	18.711
	SDSS J0843+0431	0.182	6	17.835
	EC 23487−2424	0.115	3	15.355
	Ross 808	0.112	17	14.408
	SDSS J2159+1322	−0.095	3	18.959
	TIC 167486543	−0.114	2	16.233
	SDSS J1641+3521	−0.087	2	19.092
	GALEX J1612+0830	−0.071	1	17.806
	GALEX J1257+0124	−0.077	8	18.665
	G 29−38	−0.071	38	13.062
$M_{\rm Seis}$ vs $M_{\rm Astr}$ ($\Delta M_\star \equiv M_{\rm Astr} - M_{\rm Seis}$)	2QZ J1323+0103	0.132	15	18.549
	TIC 167486543	0.139	2	16.233
	GALEX J1612+0830	0.169	3	17.806
	KIC 11911480	0.144	5	18.064
	GD 518	−0.103	3	17.244
	BPM 37093	−0.115	3	13.793
	GALEX J1650+3010	−0.147	3	18.151
	GALEX J2208+0654	−0.117	2	17.972
	GALEX J0048+1521	−0.128	6	18.711
	SDSS J0843+0431	−0.175	6	17.835
	EC 23487−2424	−0.103	3	15.355
	Ross 808	−0.090	17	14.408
$M_{\rm Spec}$ vs $M_{\rm Astr}$ ($\Delta M_\star \equiv M_{\rm Astr} - M_{\rm Spec}$)	2QZ J1323+0103	0.173	15	18.549
	GALEX J1612+0830	0.098	1	17.806
	GALEX J2208+0654	0.082	2	17.972
	GALEX J0048+1521	0.119	6	18.711
	KIC 11911480	0.117	5	18.064
	GD 518	−0.041	3	17.244
	SDSS J2159+1322	−0.131	3	18.959
	SDSS J1641+3521	−0.087	2	19.092
	GALEX J1257+0124	−0.114	8	18.665
$M_{\rm Astr}$ vs $M_{\rm Phot}$ ($\Delta M_\star \equiv M_{\rm Astr} - M_{\rm Phot}$)	GALEX J0048+1521	−0.031	6	18.711
	GALEX J1257+0124	−0.076	1	18.665
	2QZ J1323+0103	0.229	15	18.549
	SDSS J1641+3521	0.125	2	19.092
	SDSS J2159+1322	−0.047	3	18.959
$M_{\rm Phot}$ vs $M_{\rm Seis}$ ($\Delta M_\star \equiv M_{\rm Phot} - M_{\rm Seis}$)	KIC 11911480	0.049	5	18.064
	EC 23487−2424	−0.150	3	15.355
	SDSS J0843+0431	−0.243	6	17.835
	GALEX J1257+0124	0.039	1	18.665
	GALEX J1612+0830	0.125	1	17.806
	GALEX J1650+3010	−0.200	3	18.151
	BPM 37093	−0.150	3	13.793
$M_{\rm Phot}$ vs $M_{\rm Spec}$ ($\Delta M_\star \equiv M_{\rm Phot} - M_{\rm Spec}$)	EC 11507−1519	−0.102	2	16.031
	GALEX J0048+1521	0.150	6	18.711
	GALEX J1612+0830	0.054	1	17.806
	SDSS J1641+3521	−0.212	2	19.092
	GALEX J2208+0654	0.075	2	17.972

Notes. The table includes the mass differences, the number of g-mode periods employed to derive the seismological model, and their apparent brightness.